Construction and Building Materials 312 (2021) 125401

Contents lists available at ScienceDirect

Construction and Building Materials

journal homepage: www.elsevier.com/locate/conbuildmat

Confinement model for concrete wrapped with fiber reinforced cementitious mortar

Ali Hadi Adheem [a], Majid M.A. Kadhim [b], Akram Jawdhari [c,*], Amir Fam [c]

[a] Kerbala Technical Institute, Al-Furat Al-Awsat Technical University, 56001 Kerbala, Iraq
[b] University of Babylon, Hilla, Iraq
[c] Queen's University, Kingston, ON K2E 6J1, Canada

ARTICLE INFO

Keywords:
FRCM, FRP
Concrete
Confinement
Finite element
Parametric analysis
Design-oriented model

ABSTRACT

Fiber reinforced cementitious mortar (FRCM) improves the performance of fiber-reinforce polymer (FRP) by replacing the organic matrix (e.g., epoxy) with inorganic one, resulting in a more sustainable alternative with a much improved fire resistance. While numerous models have been developed for FRP-confined concrete, FRCM-confined concrete have not received nearly as much attention. This study introduces a design-oriented model for FRCM-confined concrete. The model is the first to be derived from a very large database comprising 139 experimental specimens with various geometric and material properties, complemented with additional 144 numerical specimens obtained from finite element (FE) analysis. A nonlinear three-dimensional FE model was developed and verified with experimental results. It was used to examine the effects of mortar compressive strength (f_m) and thickness (t_m), type of FRP fabric, number of FRCM layers (n), compressive strength of unconfined concrete (f_{co}), and height-to-diameter ratio (H/D). Results showed that the confined concrete strength (f_{cc}) increases linearly as f_m and t_m increase, for all examined n, f_{co}, and (H/D) values. f_{cc} also varies almost linearly with n for all fabric types. A statistical analysis was performed on the combined database and a semi-empirical confinement model was developed to predict the peak strength and corresponding strain. It provided much better statistical performance and correlation with results than existing models and included a special coefficient for the effects of mortar properties.

1. Introduction

Although known for their excellent bond, durability, and mechanical properties [1], the use of organic resins (e.g. epoxies) in binding or impregnating FRP reinforcement possesses many challenges. This includes poor behavior above the glass transition temperature, requirements for high cost fire protection systems; lack of vapor permeability and reversibility; emission of toxic substances during installation; inapplicability on moist surfaces or at low temperatures and recyclability [2–6]. This has prompted researchers to examine inorganic matrices, typically of cementitious nature, as a cost-effective and sustainable alternative [1,4,7,8]. Initial bond and impregnation challenges due to the granularity of the cement-based mortar were overcome by modifying the mortar composition, adding modifiers such as fly ash, silica fumes and polymers, and utilizing FRP in the form of textiles or open meshes instead of continuous sheets or solid plates [9]. The resulting system is widely known in literature as fiber-reinforced cementitious matrix (FRCM), although other names also exist, including: textile-reinforced mortar (TRM) and mineral-based composite (MBC) [10]. FRCM system has been used in many retrofit applications, including strengthening of concrete beams and slabs in flexure [11,12], concrete beams in shear and torsion [13,14], and masonry walls [15,16], with results showing significant increases in strength, stiffness and ductility, and reductions in crack widths and deflections.

Column confinement is an another application of FRCM systems, where they were reported to be very effective in increasing the axial strength and axial strain, showing a hardening (ascending) post-elastic stress–strain behavior similar to that seen in FRP-confined members and a much more ductile and gradual failure [4]. Triantafillou et al. [4] tested 14 cylinders, confined by FRP and FRCM jackets, and reported an effectiveness for FRCM jackets, 80% that of FRP ones. From testes on full-scale columns, FRCM was only 10% less effective than FRP [17]. Other studies examined the number of FRCM layers and fiber orientation, overlap length for final layer, concrete compressive strength, cross-

* Corresponding author.
E-mail address: akram.jawdhari@queensu.ca (A. Jawdhari).

https://doi.org/10.1016/j.conbuildmat.2021.125401
Received 11 June 2021; Received in revised form 21 October 2021; Accepted 24 October 2021

section shape, load eccentricity, slenderness, and effects of elevated temperature [1,3,4,17–20]. Recent research has also studied the strengthening of corroded [21] or damaged columns [22], anchorage aspects [23], and behavior under cyclic or seismic loading [24,25]. Fiber type for the FRP grid comprising the FRCM jacket has also been studied, comparing four materials; p-Phenylene Benzobis Oxazole (PBO), Carbon, Basalt, and Glass. The first three have high tensile strength and stiffness, and thus can provide substantial increase to member strength and ductility [2,26], although Glass-FRCM is sometimes desirable due to its cost effectiveness. However, some parameters have not been investigated, or only investigated with a limited number of specimens such as mortar properties and thickness and slenderness ratio (i.e. *H/D* ratio, where *H* is the specimen's height, and *D* is diameter).

Few studies have focused on developing analytical models to predict the stress–strain response of FRCM-confined concrete [1,3,4,19]. These models were derived using statistical fitting of experimental data and relating the axial strength to the lateral pressure induced by the FRCM jacket, which is a function of its elastic modulus, ultimate strain, and number of layers. Most of these models, except for [27], were developed based on fitting a small set of experimental data containing only a single material or geometric properties, or a limited range of for the examined parameters. Additionally, key parameters, including FRP fabric type, specimen size (height-to-diameter ratio), mortar's compressive strength, and thickness of mortar layer, were not included in the model's formulations. The aim of this study is to develop and present a design-oriented concrete confinement model for the FRCM system based on a comprehensive database that captures all the critical parameters overlooked previously, with a sufficient range for each. A large experimental database of 139 cylindrical specimens, having various material and geometrical properties, was compiled from the open literature, and used in the model development. Parameters not included in the database or not fully examined, were identified, and investigated numerically using a robust three-dimensional finite element (FE) model that has been verified using the experimental results and used in a comprehensive parametric study that added 144 additional data points.

2. Existing frcm confinement models

Several confinement models have been proposed for FRCM-confined concrete [1,3,4,28], mostly derived from limited number of test specimens and few variations in parameters. However, Ombres and Mazzuca [27] proposed a new model based on a relatively large experimental database of 152 compression tests collected from literature. The database was used to evaluate the performance of other existing FRCM confinement models, where they found that models developed by De Caso y Basalo, et al. [1], Ombres [3], Triantafillou, et al. [4] are largely unconservative in most cases, while the model proposed in ACI 549 guide [28] furnished reasonable predictions.

2.1. ACI 549 model [28]

The peak concrete compressive strength (f_{cc}) and corresponding axial strain (ε_{cc}) in this model can be calculated using Eqs. (1) and (2) as follows:

$$\frac{f_{cc}}{f_{co}} = 1 + 3.1\left(\frac{f_{lu}}{f_{co}}\right) \tag{1}$$

$$\frac{\varepsilon_{cc}}{\varepsilon_{co}} = 1 + 12\left(\frac{f_{lu}}{f_{co}}\right)\left(\frac{\varepsilon_{fe}}{\varepsilon_{co}}\right)^{0.45} \leq 0.01 \tag{2}$$

where f_{co} is the peak compressive strength of unconfined concrete, ε_{co} is the maximum axial strain of the unconfined concrete, f_{lu} is the maximum confinement pressure, and ε_{fe} is effective tensile strain in the FRCM. The value of f_{lu} and ε_{fe} can be calculated using Eqs. (3) and (4), respectively:

$$f_{lu} = \left(\frac{2nA_f E_f \varepsilon_{fe}}{D}\right) \tag{3}$$

$$\varepsilon_{fe} = \varepsilon_{fd} \leq 0.012 \tag{4}$$

where n is the number of FRCM layers, A_f is the area of FRP reinforcement per unit width, E_f is the FRP elastic modulus, D is the diameter of the circular section, and $\varepsilon_{fd} = \varepsilon_{fu}$ where ε_{fu} is the ultimate tensile strain of the FRP fibers. The strain efficiency factor (k_ε) that is typically used in confinement models for FRP jackets [28] is not considered in Eq. (4) for FRCM system.

2.2. Ombres and Mazzuca model [27]

As stated previously, this model was derived from best-fit analysis of an experimental database of 152 compression tests, covering a range of parameters including FRP type, concrete compressive strength, and properties of mortar. The values of (f_{cc}) and (ε_{cc}) can be calculated from Eqs. (5) and (6) as follows:

$$\frac{f_{cc}}{f_{co}} = 1 + 0.913\left(\frac{f_{lu}}{f_{co}}\right)^{0.5} \tag{5}$$

$$\frac{\varepsilon_{cc}}{\varepsilon_{co}} = 1 + 0.963\left(\frac{f_{lu}}{f_{co}}\right)\left(\frac{\varepsilon_{fe}}{\varepsilon_{co}}\right)^{0.5} \tag{6}$$

where the values of f_{lu} and ε_{fe} can be calculated as in Eqs. (7) and (8), respectively.

$$f_{lu} = \frac{k_e k_\theta \rho_f E_f \varepsilon_{fu}}{2} \tag{7}$$

$$\varepsilon_{fe} = k_e \varepsilon_{fu} \tag{8}$$

where k_e and k_θ are coefficients relating to the strain efficiency of FRCM jackets and fiber orientation (θ), respectively, and can be calculated using Eqs. (9) and (10), as follows:

$$k_e = 0.25\left[\left(\frac{\rho_f E_f}{f_{co}}\right)^{0.3} - 1\right] \tag{9}$$

$$k_\theta = \frac{1}{1 + 3tan\theta} \tag{10}$$

Eq. (9) shows that k_e is affected by the material and geometric properties of the FRCM jacket and is proportional to the jacket volumetric reinforcement ratio (ρ_f), calculated as ($\rho_f = 4nt_f/D$), where t_f is the thickness of the fabric grid, while n and D, have already been defined.

3. Experimental database

In this study, a comprehensive FE model was developed to examine the performance of FRCM-confined concrete beyond the existing experimental database and establish the full effects of several parameters that are not included experimentally or overlooked in other models. The model predictions were compared with the results of 33 compression tests performed on cylindrical and prismatic (square) concrete specimens confined with FRCM jackets, reported from literature [2–4,26,29,30]. The experimental specimens were carefully selected to represent a wide range of variables related to the behavior of FRCM confinement. The diameter (D) varied between 113 and 200 mm and the height (H) ranged from 290 to 425 mm (i.e. H/D ratio of 1.68 to 2.65). The compressive strength of unconfined concrete (f_{co}) ranged from 15.2 to 29.2 MPa. The specimens were confined with different types of fabric materials including carbon (CFRCM), for 8 specimens; glass (GFRCM), for 4 specimens; basalt (BFRCM), for 4 specimens; and p-Phenylene

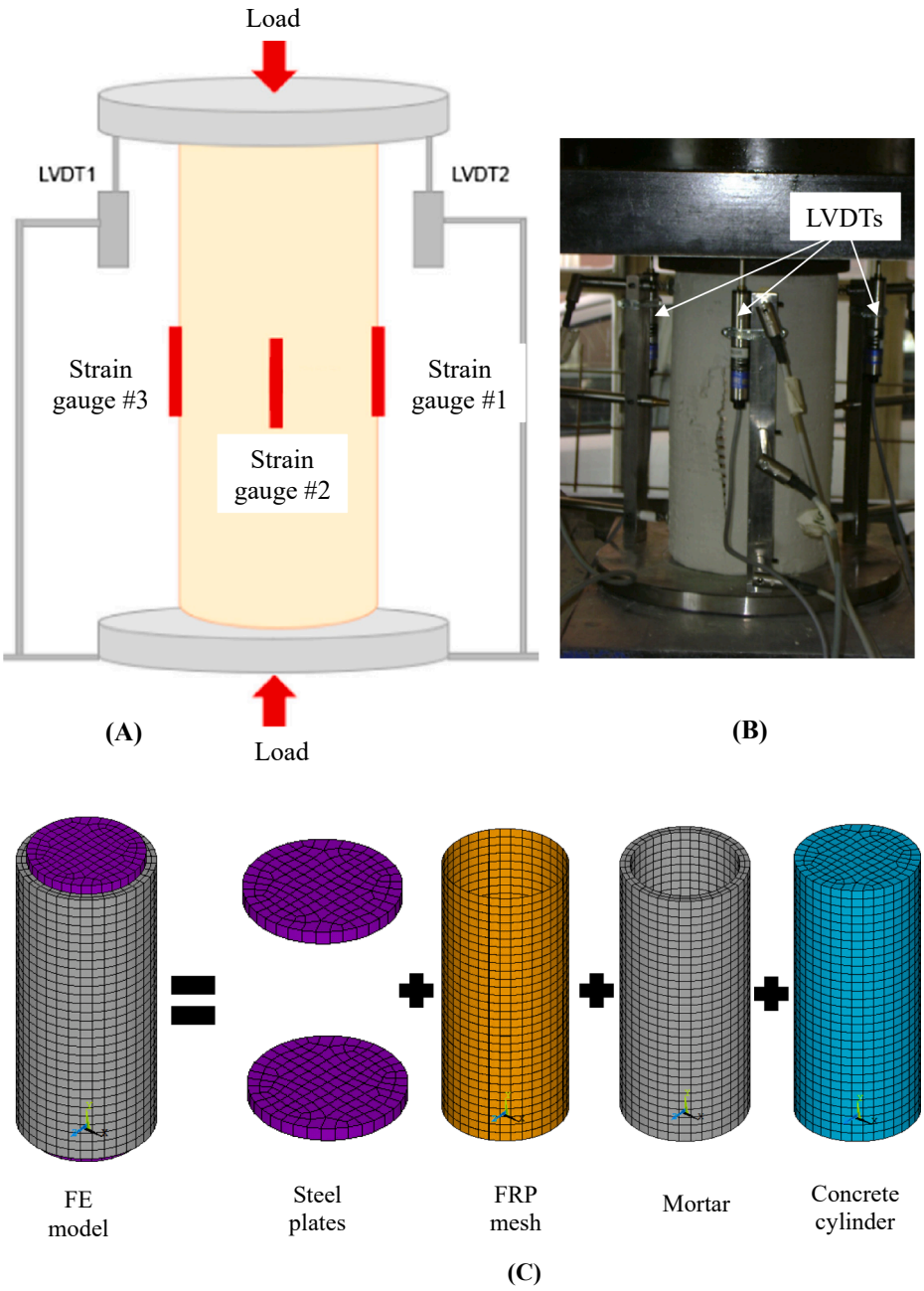

Fig. 1. (A) Schematics of test setup and instrumentation [8]; (B) photo of specimen undergoing testing [3], and (C) typical FE model of FRCM-confined concrete cylinder.

Benzobis Oxazole (PBO-FRCM), for 17 specimens. The number of fabric mesh layers (n) used in FRCM composite system ranged from 1 to 4.

The validation specimens were all un-reinforced (plain) concrete and were tested under uniaxial compression applied monotonically and concentrically. Application of FRCM jacketing system commenced by dampening the concrete surface, then applying the first mortar layer, followed by the FRP grid which was pressed gently forcing the mortar to flow through the perforations between fiber rovings. A covering mortar layer is applied then and the same operation is repeated if multiple textile layers are to be used. The specimens are typically instrumented with a load cell to record the load which is divided by area to calculate stress and by extensometers, Linear Potentiometers, or Linear Variable Differential Transducers (LVDTs) to measure strains in longitudinal and hoop directions.

4. Finite element model development

This section summarizes the FE model development including element types, material properties and mesh sensitivity analysis. The numerical models for FRCM-confined concrete specimens were developed in the commercial FE software ANSYS APDL 17.2 [31], using a three-dimensional modeling approach and considering the full size of the specimen. The load was applied by an imposed displacement over the top steel plate to resemble a displacement-controlled scheme which is typically more robust than force-controlled loading and can simulate post-peak response [5]. The Newton-Raphson solution method was utilized by incrementing the load in small automatic steps and iterating until the cumulative force vector becomes smaller than a specified convergence criterion of 5% [32].

Table 1
Properties of FRCM-confined concrete specimens used in FE model validation.

ID	f_{co} (MPa)	D (mm)	H (mm)	H/D	fabric type	n	E_m(GPa)	E_f (GPa)	t_m(mm)	f_m(MPa)	f_f(MPa)	Ref.
1	22.6	113	300	2.65	PBO	1	6	270	8	16.00	5800	[30]
2	22.6	113	300	2.65	PBO	2	6	270	12	16.00	5800	
3	22.6	113	300	2.65	PBO	3	6	270	16	16.00	5800	
4	15.4	152	290	1.91	PBO	1	6.1	270	6	30.40	5800	[3]
5	15.4	152	290	1.91	PBO	2	6.1	270	9	30.40	5800	
6	15.4	152	290	1.91	PBO	3	6.1	270	12	30.40	5800	
7	15.4	152	290	1.91	PBO	4	6.1	270	15	30.40	5800	
8	29.3	152	290	1.91	PBO	1	6.1	270	6	30.40	5800	
9	29.3	152	290	1.91	PBO	2	6.1	270	9	30.40	5800	
10	29.3	152	290	1.91	PBO	3	6.1	270	12	30.40	5800	
11	29.3	152	290	1.91	PBO	4	6.1	270	15	30.40	5800	
12	24.2	154	335	2.18	PBO	2	6.0	270	6	15.00	5800	[29]
13	24.2	154	335	2.18	PBO	3	6.0	270	9	15.00	5800	
14	24.4	200	335	1.68	PBO	2	6.0	270	6	15.00	5800	
15	24.4	200	335	1.68	PBO	3	6.0	270	9	15.00	5800	
16	25.5	B = 200	425	2.13	PBO	2	6.0	270	6	15.00	5800	
17	25.5	B = 200	425	2.13	PBO	3	6.0	270	9	15.00	5800	
18	15.0	100	200	2.00	C	2	6.1	242	12	22.90	1487	[2]
19	15.0	154	300	1.95	C	2	6.1	242	12	22.90	1487	
20	15.0	154	300	1.95	G	2	6.1	57	12	22.90	586	
21	15.5	150	300	2.00	G	2	6.1	72	12	30.00	1440	[26]
22	17.8	150	300	2.00	G	1	6.1	72	8	30.00	1440	
23	17.8	150	300	2.00	G	2	6.1	72	12	30.00	1440	
24	15.5	150	300	2.00	B	1	6.1	91	8	30.00	1814	
25	15.5	150	300	2.00	B	2	6.1	91	12	30.00	1814	
26	17.8	150	300	2.00	B	1	6.1	91	8	30.00	1814	
27	17.8	150	300	2.00	B	2	6.1	91	12	30.00	1814	
28	15.2	150	300	2.00	C	2	6.0	225	6	8.56	3350	[4]
29	15.2	150	300	2.00	C	3	6.0	225	8	8.56	3350	
30	15.2	150	300	2.00	C	2	6.0	225	6	30.61	3350	
31	15.2	150	300	2.00	C	3	6.0	225	8	30.61	3350	
32	21.8	150	300	2.00	C	2	6.0	225	6	30.61	3350	
33	21.8	150	300	2.00	C	3	6.0	225	8	30.61	3350	

f_{co} = compressive strength of unconfined concrete; D = specimen diameter; B = width of square cross section, H = specimen height; n = number of the fabric meshes; E_f = FRP elastic modulus; E_m = elastic modulus of mortar; t_m: mortar thickness; f_m = compressive strength of mortar; f_f = tensile strength of FRP fabric.

4.1. Element types

The concrete core and steel plates, which were added at the top and bottom of the specimen to simulate capping and minimize edge failure due to stress concentrations, were modeled with the 8-node brick element SOLID185. This element has three translational degrees of freedom (DOF) per node, and can be used to represent various nonlinear properties such as plasticity, stress stiffening, large deformations, and large strains [32]. To simulate mortar cracking which was a frequently observed failure mode in the tested samples, the mortar layer was modeled as a discrete solid part having a thickness (t_m) as reported from the tests. Also, the mortar is expected to contribute to confinement, particularly before it cracks. SOLID65, an 8-node brick element with 3 translational DOFs, was used to model the mortar. The element was chosen because of its special capability of representing concrete and inclusion of cracking and crushing algorithms [31].

The FRP grid/mesh within the FRCM jacket was modeled as a shell, using SHELL181 element which has four nodes, three translational DOFs, three rotational DOFs, and both membrane and bending capabilities [31]. The element allows for stacking of up to 250 layers, each with a separate thickness, orientation, and material type. Following the approach implemented in multiple studies, the FRP open grid was smeared into a continuous fabric layer with an equivalent thickness determined from equating its axial stiffness to that of the grid [5,14,33]. Because the FRCM-to-concrete interface is continuously under compressive stresses due to dilation of concrete under axial loading, the bond-slip relation and debonding of FRP and FRCM-confined columns are not critical as for the case in strengthened concrete members under flexural or shear loads [34–39]. Therefore, a full bond condition was assumed between the fiber mesh and mortar and between the entire FRCM system and concrete core and idealized by merging coincident nodes.

In case more than one FRCM layer is used and to simplify the analysis, the multiple layers were replaced with a single fabric layer embedded at mid thickness of one mortar layer. The thicknesses of the idealized fabric (t_a) and mortar (t_m) were obtained by summing the thicknesses of the multiple layers. Fig. 1 shows the FE model and various components for a typical FRCM-confined concrete cylinder, alongside the test setup and instrumentation for a typical specimen.

4.2. Material properties

The concrete core was modeled with the Drucker-Prager Concrete (DPC) model, a new member of DP models, developed in recent ANSYS versions such V17.2. DPC model takes into account the concrete dilation under axial compression and unlike traditional DP models, it has a separate yield criterion for tension and compression failures, a nonlinear stress–strain response in compression, and several hardening/softening rules [5,31]. The authors had previously implemented the DPC model in simulating the axial response of slender FRCM-confined RC columns under eccentric loading and obtained good correlation with test results [5]. The DPC model could not be implemented from ANSYS graphical user interface (GUI) but was added as a command subroutine. Other inputs required in the DPC model are concrete elastic modulus (E_c), tensile strength (f_t), and Poisson's ratio (ν). f_t and E_c were calculated as $f_t = 0.625\sqrt{f_c^{'}}$ and $E_c = 4700\sqrt{f_c^{'}}$ following ACI-318 code [6,40,41], while ν was assumed to be 0.2 [5,41,42]. The added steel loading and bearing plates were modeled as linear elastic material, with a modulus of elasticity (E_s) of 200 GPa and (ν) of 0.3.

The mortar was simulated by the concrete plasticity (CP) model associated with SOLD65. The model utilizes a five-parameter William and Warnke failure criteria [43], and considers cracking and crushing

Table 2
Key test and numerical comparisons for validating the developed FE model.

ID	f_{co} (MPa)	f_{cc}–Exp. (MPa)	f_{co}/f_{cc} (Exp)	f_{cc}–FEM (MPa)	f_{co}/f_{cc} (FEM)	f_{cc} Exp./ f_{cc} FE	ε_{cc}–Exp. (%)	ε_{cc}–FEM (%)	Exp./FE
1	22.6	32.65	0.69	33.94	0.67	0.96	0.69	0.70	0.99
2	22.6	43.51	0.52	44.50	0.51	0.98	1.15	1.31	0.88
3	22.6	56.74	0.40	51.22	0.44	1.11	1.71	1.31	1.31
4	15.4	24.64	0.63	22.73	0.68	1.08	1.18	1.34	0.88
5	15.4	35.29	0.44	34.11	0.45	1.03	2.00	2.53	0.79
6	15.4	41.70	0.37	41.04	0.38	1.02	2.94	2.74	1.07
7	15.4	49.23	0.31	48.01	0.32	1.03	2.67	2.89	0.92
8	29.3	43.49	0.67	39.14	0.75	1.11	0.73	2.54	0.29
9	29.3	46.60	0.63	44.66	0.66	1.04	1.45	1.82	0.80
10	29.3	56.45	0.52	53.27	0.55	1.06	1.96	2.46	0.80
11	29.3	56.67	0.52	55.88	0.52	1.01	2.15	1.98	1.09
12	24.2	30.60	0.79	31.70	0.76	0.97	1.16	1.13	1.03
13	24.2	36.20	0.67	33.46	0.72	1.08	1.14	1.58	0.72
14	24.4	29.00	0.84	30.18	0.81	0.96	1.14	1.06	1.08
15	24.4	34.70	0.70	32.28	0.76	1.07	0.92	1.13	0.81
16	25.5	26.10	0.98	27.20	0.94	0.96	0.38	1.10	0.35
17	25.5	30.20	0.84	29.55	0.86	1.02	0.52	1.33	0.39
18	15.0	18.31	0.82	20.32	0.74	0.90	0.14	0.54	0.26
19	15.0	22.40	0.67	23.20	0.65	0.97	0.50	0.59	0.85
20	15.0	20.11	0.75	21.50	0.70	0.94	0.16	0.58	0.28
21	15.5	22.42	0.69	20.11	0.77	1.11	0.30	1.88	0.16
22	17.8	21.87	0.82	20.83	0.86	1.05	0.40	1.73	0.23
23	17.8	22.97	0.78	22.32	0.80	1.03	0.41	1.86	0.22
24	15.5	22.66	0.68	20.78	0.75	1.09	0.31	0.88	0.35
25	15.5	23.10	0.67	23.33	0.67	0.99	0.64	0.93	0.69
26	17.8	26.31	0.68	24.46	0.73	1.08	0.40	1.53	0.26
27	17.8	28.69	0.62	25.74	0.69	1.11	0.62	1.03	0.60
28	15.2	20.17	0.76	21.51	0.71	0.94	1.23	1.23	1.00
29	15.2	25.88	0.59	25.94	0.59	1.00	1.16	1.33	0.87
30	15.2	23.14	0.66	24.35	0.63	0.95	1.08	1.18	0.92
31	15.2	28.50	0.53	28.38	0.54	1.00	1.27	1.23	1.03
32	21.8	27.82	0.78	30.70	0.71	0.91	1.01	1.13	0.89
33	21.8	33.11	0.66	33.22	0.66	1.00	1.08	1.28	0.84
Mean						1.02			0.72
Coefficient of variation %						5.95			44.97

f_{co} = compressive strength of unconfined concrete; f_{cc} and ε_{cc} = peak compressive strength of confined concrete and the corresponding axial strain respectively.

failures. Material properties required to populate the model, including the mortar compressive strength (f_m) and its elastic modulus (E_m), were taken from the experimental studies, as reported in Table 1. The mortar tensile strength ($f_{m\text{-}t}$) was calculated as $f_{m-t} = 0.625\sqrt{f_m}$ [40]. The open and closed shear crack parameters, relating to the magnitude of shear forces transferred across the face of a crack for loading and unloading stages, respectively, were both assumed to be 0.3 [5,6,42]; while v was taken as 0.2.

The FRP grid was modeled as an orthotropic elastic material until failure. Table 1 lists the tensile strength (f_f) and elastic modulus (E_f) in the fiber direction, for the fabrics used in the experimental studies. Other material properties, including the transverse elastic moduli, shear moduli, and Poisson's ratios, were not reported in the tests, but were taken from [42,44] assuming typical FRP types and fiber volume fractions. FRP rupture was explicitly simulated using a composite damage mechanics (CDM) model and Maximum Stress failure criteria. The rupture initiated when the stress exceeded f_f and progressed by degrading the fabric stiffness by a factor of 0.99 to simulate the brittle failure of FRP composites. Further details into the CDM model can be found in Jawdhari and Fam [42].

4.3. Mesh sensitivity analysis

Various mesh sizes were examined to arrive at a mesh that provides a good balance between computational efforts and accuracy. A mesh with an element side length of 10 mm for all parts (concrete, fabric, and mortar) was found sufficient and provided a divergence in maximum stress of less than 1%, when compared with smaller size meshes.

5. Validation of Fe model

Predictions of the FE model were compared with results of the experiments discussed earlier and reported in Table 1. The comparisons included the axial stress–strain curve, peak compressive strength and the corresponding axial strain, and failure pattern.

5.1. Peak strength and axial strain

The experimental and FE model peak compressive strength of the confined concrete (f_{cc}) and corresponding axial strain (ε_{cc}) are compared in Table 2. It can be observed that f_{cc} is significantly affected by several factors, including the number of fabric layers, the type of fabric and the compression strength of unconfined concrete. The trend is the same for both experimental and FE results. It can also be seen from Table 2 that the maximum difference between experimental and FE values of f_{cc} was 11% occurring in four specimens (#3, 8, 21, and 27), with an average difference of 2% for all 35 specimens. Although the FE deviation from test results is within acceptable limits and is significantly smaller than the 40% maximum difference reported for FRP-confined concrete columns in [45,46], the results may be affected by factors related to the experiments such as unintended eccentricities and differences between actual and reported material and geometric properties, or to the FE model including mesh size and material idealization.

The comparisons for ε_{cc} showed an average ratio between experimental and numerical results of 0.72 for all 35 specimens. In several specimens, the experimental/numerical ε_{cc} ratio was unexpectedly low and varied between 0.16 and 0.39. The larger divergence in ratio seen in these specimens might be attributed to quality control issues in the tests, effects of curvature on rupture strain of the FRP grid, misalignment or malfunctioning of the gage, load eccentricity, cracking in the vicinity of

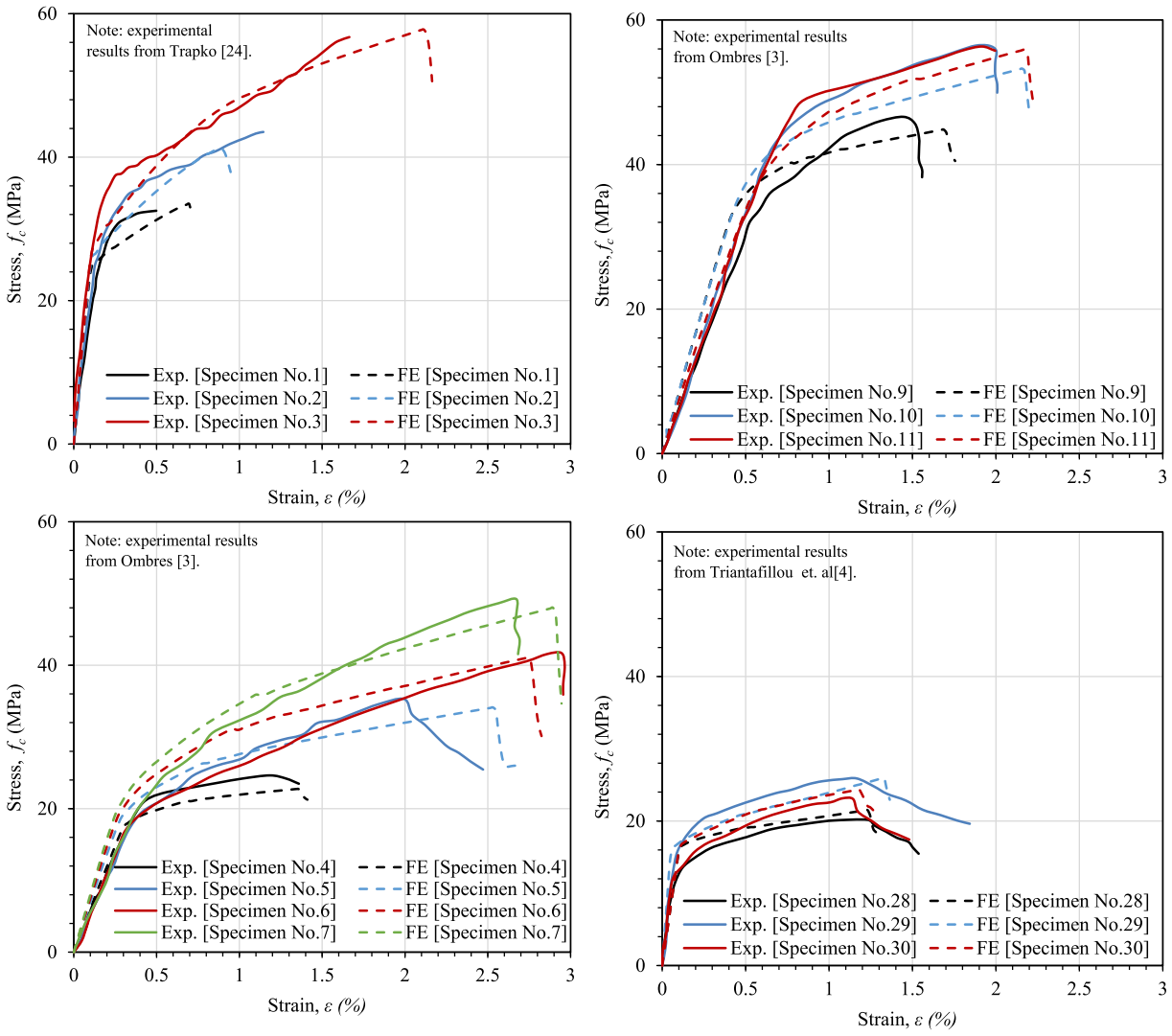

Fig. 2. Compressive stress–strain curves for selected specimens, from tests and FE models (specimen number refers to the identification in Table 1).

the strain gage, or limitations in the FE model such as those discussed earlier. Besides numerical results, experimental data seem to also show noticeable variation in reported ε_{cc} such as in specimens #18 and 19, which have identical material properties, strengthening system, and H/D ratio. Similar differences in ε_{cc} have also been reported for FRP-confined columns [45]. In light of above discussion, the results of ε_{cc} should be viewed cautiously in the context of the geometric and material properties studied herein; while further research could be conducted to refine the analysis and provide more understanding to this variation.

5.2. Stress-strain response and failure mode

The comparison between test and FE model results for the stress–-strain curves of FRCM-confined concrete specimens are presented in Fig. 2, for 13 representative samples. It can be seen from this figure that the FE model was able in most cases to capture the entire stress–strain curve with reasonable accuracy. Although the FE predictions were somewhat stiffer in some cases compared to experimental responses, the divergence is less than 13% in terms of stress response along the entire curves. Overall, Fig. 2 shows the excellent ability of the model to capture the confinement effects of FRCM and predicting the effects of various parameters on confinement, such as specimen size, concrete strength, number of FRCM layers and type and stiffness of the FRP grid.

The FRCM-jacketed concrete specimens failed in two stages: first by exhibiting a wide crack in the mortar layer, mostly in the proximity of the overlap zone; followed by rupturing of the FRP grid due to excessive hoop stresses. In some cases, a combination of debonding failure occurring at the interface between the FRP grid and the cementitious mortar and fabric tearing, also occurred. Fig. 3 shows pictures of after-failure conditions for several specimens, along with the finite element contours of principal strains in the mortar layer (in reference to mortar cracking failure) and the Hashin failure indices representing different rupture failure levels in the grid, for various types of FRCM jackets. As can be seen, the model was able to simulate the governing failure modes, showing large principal strains in mortar at respective locations of mortar cracking failure, and a Hashin index of 1.0 (regions with red color) for the FRP grid at locations with FRP rupture failure. Of the two failure modes, the FE model showed that FRP rupture was the main cause for the sharp drop in stress–strain curve at the peak stress seen in Fig. 2. Based on the above discussions, it can be concluded that the FE model is able to capture the complete behavior of FRCM reinforced concrete elements and that it can be used in a comprehensive parametric study to enhance the database available to develop a design model.

6. Parametric study

To provide a comprehensive understanding of the variables affecting the confinement effectiveness of FRCM system and extend the relatively

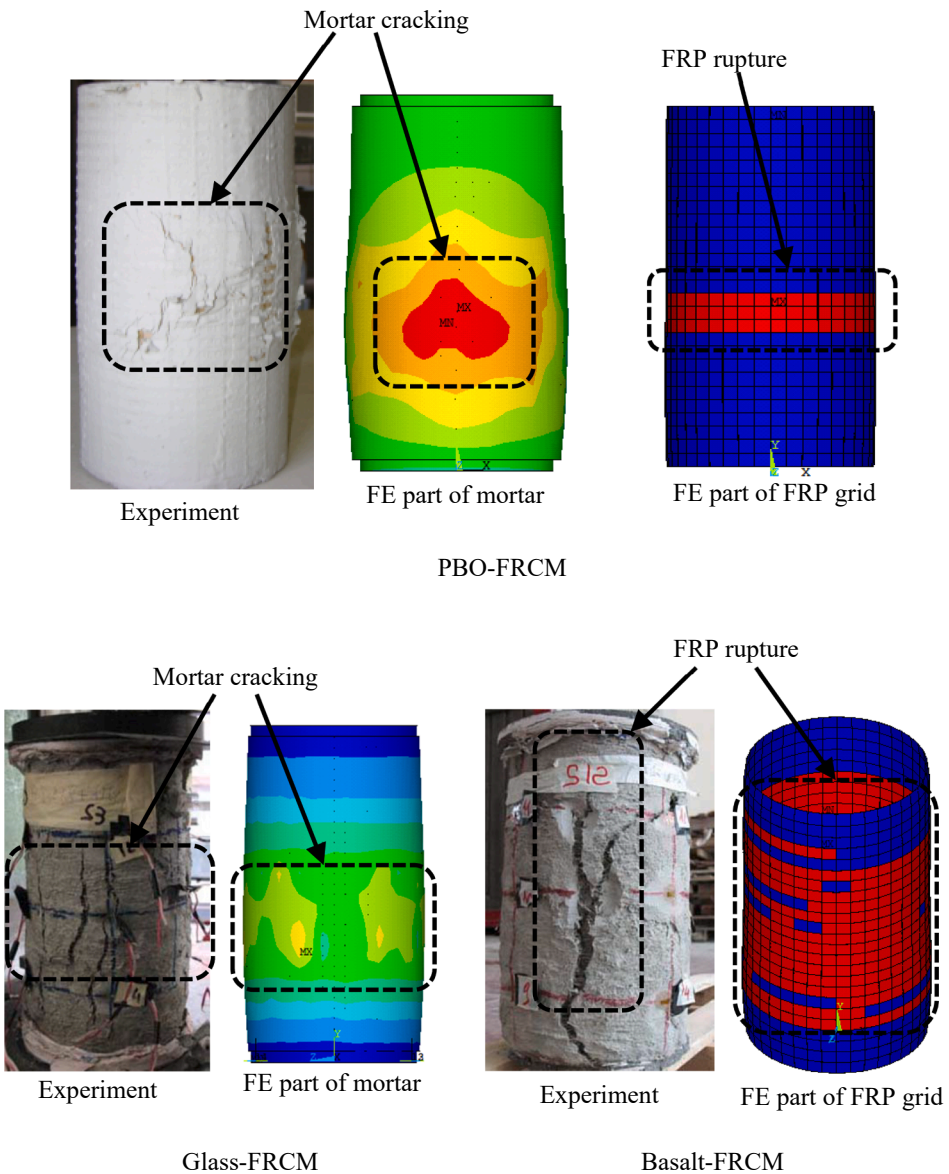

Fig. 3. Finite element prediction of governing failure modes in FRCM-confined concrete.

limited database, several parameters are investigated in this section including: the compressive strength of mortar (f_m), thickness of mortar layer (t_m), and type of FRP fabric. These parameters are studied in conjunction with the number of FRCM layers (n), compressive strength of unconfined concrete (f_{co}) and height-to-diameter ratio (H/D) for cylindrical specimens. Four values of f_m are examined, including 10, 20, 30 and 40 MPa; each coupled with five consecutive values of (n) from 1 to 5, three values of f_{co}, namely 20, 30 and 40 MPa; and four (H/D) ratios, namely 1.5, 2, 2.5, and 3. The parametric study was performed on a cylindrical specimen with a constant diameter of 150 mm, and except when varying the individual variable, with a height of 300 mm (H/D = 2), f_{co} of 30 MPa, n = 2, f_m of 20 MPa, t_m of 4 mm, and E_f = 270 GPa (PBO-FRCM).

6.1. Effect of compressive strength of mortar (f_m)

A total of 40 specimens are analyzed in this section for f_m ranging from 10 to 40 MPa. The results are presented in terms of the most important parameters, namely f_{cc} and ε_{cc}, which are crucial for development of a new confinement model, or the evaluation of existing ones. Fig. 4 plots the relation between f_{cc} and f_m, for various values of n, f_{co} and (H/D) ratio. The figure shows that f_{cc} is increasing almost linearly as f_m increases, for all examined n, f_{co}, and (H/D) values, although not always by the same rate. For each individual f_m value, f_{cc} is increasing as n and f_{co} increase, but is not affected by H/D ratio. For example: when f_m is varied from 10 to 40 MPa, f_{cc} increased by 13% for the case n = 5; by 10% for f_{co} = 30 MPa, and by 10% for all H/D ratios. These values indicate that the effects of the mortar's compressive strength, which are normally neglected in the available FRCM confinement models, need to be considered. The other parameters are also very important. For example: for f_m = 20 MPa, f_{cc} increased by 46% when n is varied from 1 to 5, and by 69% when f_{co} is varied from 20 to 40 MPa.

These observations are consistent with the findings of Traintafillou et al. [4] which included only four specimens having two variations for n and f_m. The increase in f_{cc} because of increasing f_m is partially caused by the axial strength contribution provided by the mortar with the higher (f_m). This was also observed by Di Ludovico, et al. [26] which tested two concrete specimens confined with mortar only and found a 5% average increase in f_{cc}, without the fabric contribution. In addition, using higher strength mortars improves the FRCM confinement system substantially by preventing or delaying mortar cracking and stress concentrations in the FRP grid, fabric rupture, and debonding at the mortar-FRP interface.

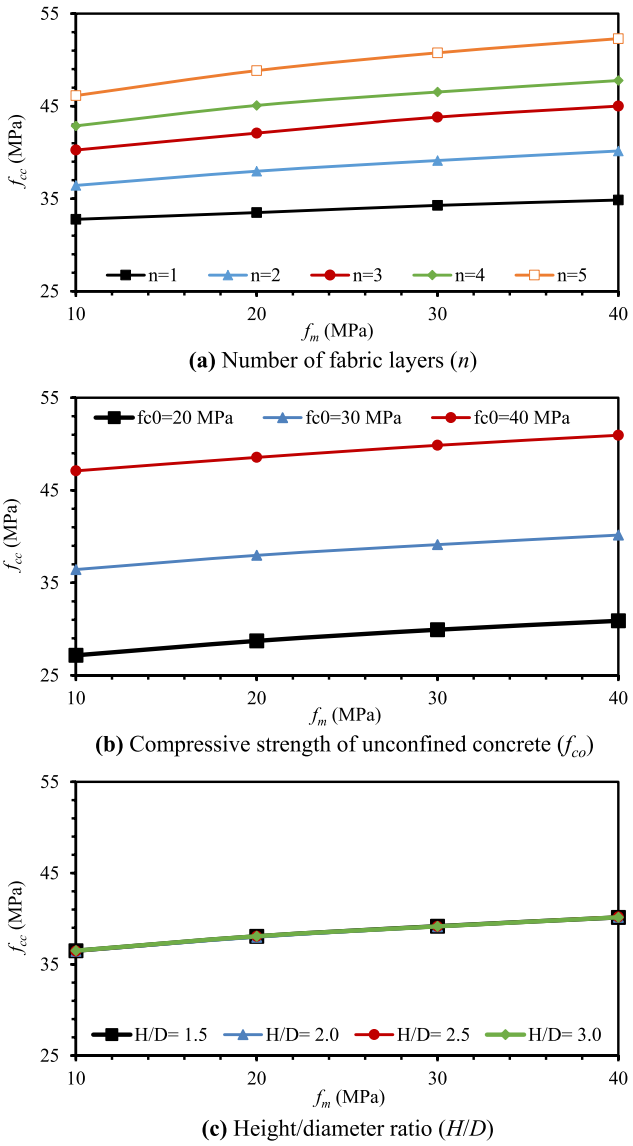

(a) Number of fabric layers (n)

(b) Compressive strength of unconfined concrete (f_{co})

(c) Height/diameter ratio (H/D)

Fig. 4. Effects of mortar compressive strength (f_m) coupled with other parameters on (f_{cc}) of confined specimens.

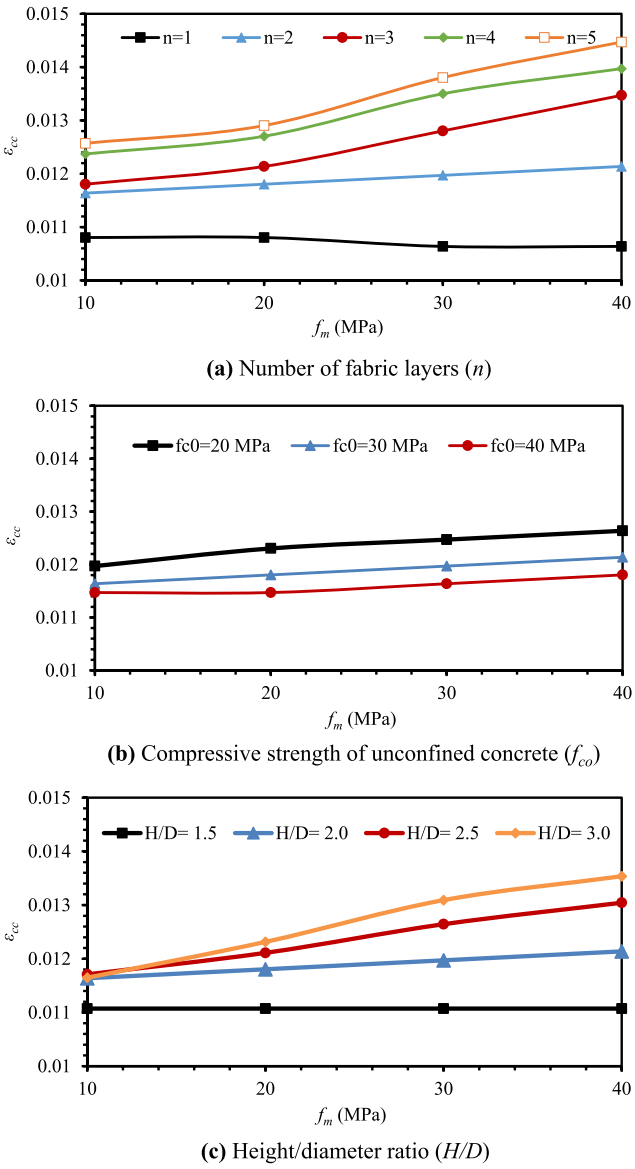

(a) Number of fabric layers (n)

(b) Compressive strength of unconfined concrete (f_{co})

(c) Height/diameter ratio (H/D)

Fig. 5. Effects of mortar compressive strength (f_m) coupled with other parameters on (ε_{cc}) of confined specimens.

Similar to Fig. 4, Fig. 5 plots the relation between ε_{cc} and f_m, for a range of values of n, f_{co}, and (H/D) ratio. The figure shows a different trend to what was observed for f_{cc}, where in Fig. 5, ε_{cc} seems to increase with f_m for most n, f_{co}, and (H/D) values, but not always linearly or by the same rate. Particularly, ε_{cc} was approximately constant in relation to f_m, when $n = 1$ and $H/D = 1.5$, but it started to increase rapidly with f_m when n and H/D increased. The (ε_{cc}-f_m) relation shows a more consistent linear trend, when f_{co} is the secondary variable (Fig. 5(b)). Also, unlike peak compressive strength, ε_{cc} in Fig. 5 seems to vary with H/D ratio.

6.2. Effect of mortar thickness (t_m)

Three different mortar thicknesses were investigated, namely 2, 6 and 8 mm, in addition to the $t_m = 4$ mm used earlier. The effects of this parameter is also examined in combination with the three secondary variables, n, f_{co}, and H/D ratio. The simulation results are shown in Fig. 6 which shows that an increase in t_m causes a linear increase in f_{cc}, for all n, f_{co}, and (H/D) values, possibly due to the same effects discussed for the mortar strength. For each individual t_m value, f_{cc} increases as n and f_{co} increase, but is not affected by H/D ratio. For example, when t_m is varied from 2 to 8 mm, f_{cc} increased by 7.5% for $n = 5$; by 12% for $f_{co} = 30$ MPa, and by 11% for all H/D ratios. For $t_m = 6$ mm, f_{cc} increased by 45% when n is varied from 1 to 5, and by 67% when f_{co} is varied from 20 to 40 MPa. Interestingly, thickness of the mortar layer, a parameter that is not typically included in current FRCM confinement models, seems to have large effects on the compressive strength of FRCM confined concrete. The reason for the negligible effect of H/D ratio on the f_{cc} is related to the fact that the confining pressure were seen to be independent of the H/D ratio. Similar observations were also noted by Thériault, et al. [47] who investigated the effects of size and slenderness ratio on FRP-confined concrete columns.

Similarly, Fig. 7 plots the relation between ε_{cc} and t_m. The figure shows that the relation between ε_{cc} and t_m is nonlinear, with ε_{cc} appearing to increase until $t_m = 6$ mm, then it either flattens or decreases at $t_m = 8$ mm, for all n, f_{co}, and (H/D) values. The flattening/decreasing trend at $t_m = 8$ mm might be caused by the brittle cracking failure dominating in thick mortar layers and affecting the rupture strain of the embedded FRP grid.

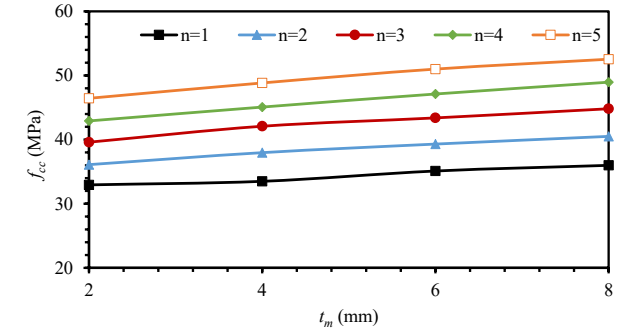

(a) Number of fabric layers (n)

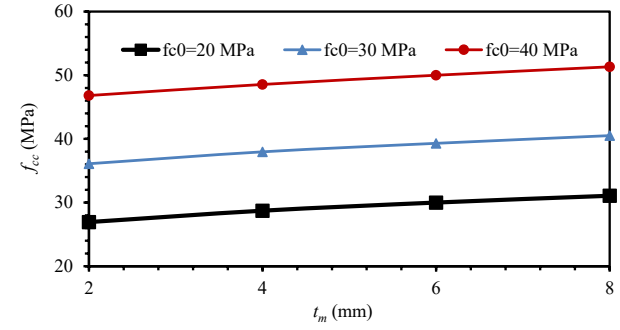

(b) Compressive strength of unconfined concrete (f_{co})

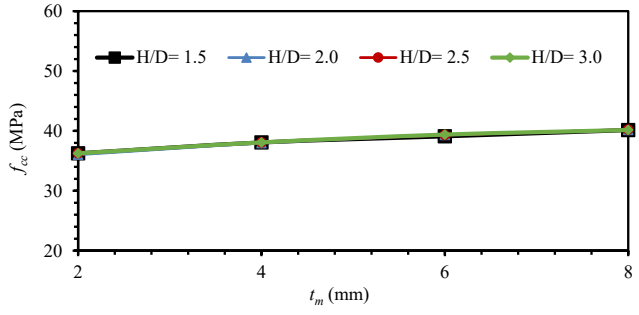

(c) Height/diameter ratio (H/D)

Fig. 6. Effects of mortar thickness (t_m) coupled with other parameters on (f_{cc}) of confined specimens.

6.3. Type of FRP fabric

Most existing FRCM confinement models were derived from tests conducted on a single type of FRP fabric. To examine the effects of the fabric type on the response and confinement model of FRCM-confined concrete when it is combined with the effects of other parameters (n, f_{co}, and (H/D) ratio), four commercially available and widely used fabrics were examined, namely: PBO, Carbon, Glass, and Basalt fibers. The equivalent fabric thickness, discussed earlier, was assumed constant for all fabrics, at 0.0455 mm. Mechanical properties of each of the four fabrics, which were required as inputs for the FE models, were taken from the available literature and listed in Table 3. While multiple properties are reported in the table for each FRCM system corresponding to different systems used in the validation section, only single set of properties was selected and used for each type in the parametric study and identified in the table.

The relation between (f_{cc}) and number of FRCM layers (n) in Fig. 8(a) shows that, for all fabric types, that f_{cc} varies almost linearly with n. For example, f_{cc} of PBP-FRCM confined concrete cylinders increased by 33% when n is increased from 1 to 5. It can also be seen from this figure that the PBO-FRCM system is more effective than other types, followed by CFRCM, BFRCM, and GFRCM, corresponding to the same order of

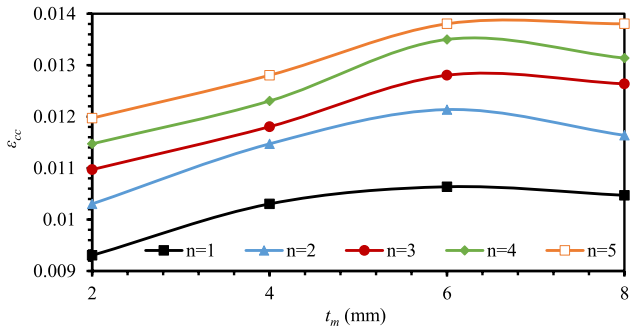

(a) Number of fabric layers (n)

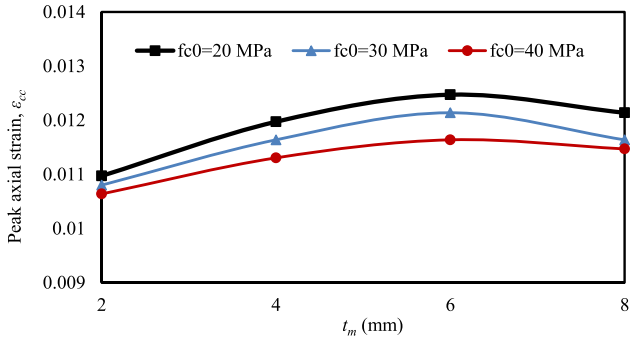

(b) Compressive strength of unconfined concrete (f_{co})

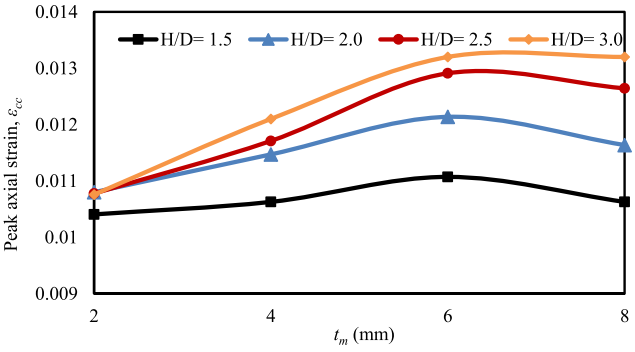

(c) Height/diameter ratio (H/D)

Fig. 7. Effects of mortar thickness (t_m) coupled with other parameters on (ε_{cc}) of confined specimens.

Table 3
Mechanical properties of FRP fabrics used in FE modelling.

Fabric type	E_f [1] (GPa)	f_{fu} [1] (MPa)	ε_{fu} [1] (%)	Reference
PBO-FRCM	270.0	5800	2.15	[3,29,30]
CFRCM[2]	225.0	3350	1.49	[4]
CFRCM	242.0	1487	1.10	[2]
CFRCM	240.0	3404	1.42	[48]
GFRCM	57.0	586	1.50	[2]
GFRCM[2]	72.0	1440	2.00	[26]
GFRCM	72.4	3240	4.48	[1]
BFRCM[2]	91.0	1814	2.00	[26]
BFRCM	52.0	894	2.20	[7]

[1] E_f = elastic modulus of fibers; f_{fu} = ultimate tensile strength of fibres; and ε_{fu} = ultimate tensile strain of fibers.

[2] Used in the parametric study as a representative of the particular FRCM system.

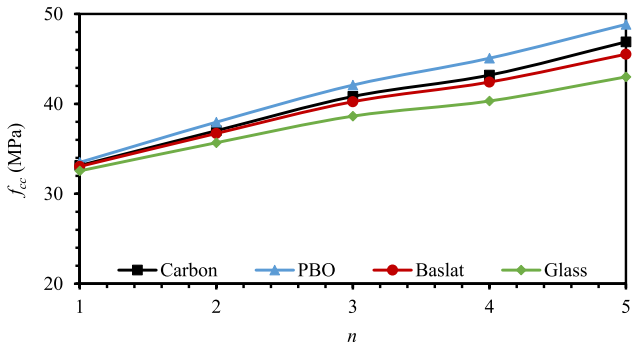

(a) Number of FRP fabric layers (n)

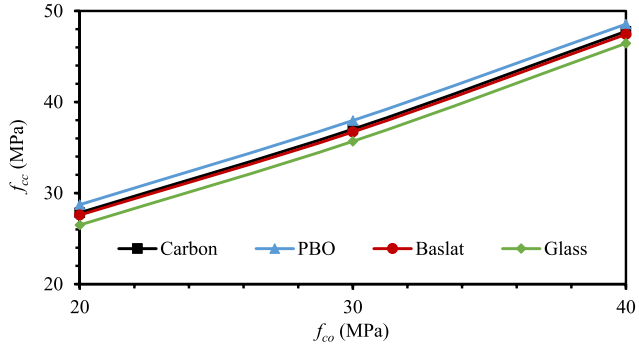

(b) Compressive strength of unconfined concrete (f_{co})

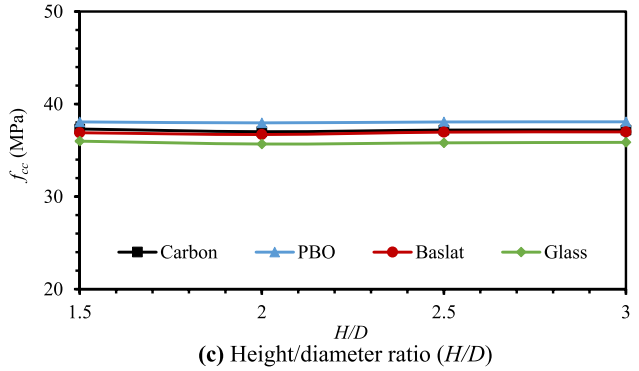

(c) Height/diameter ratio (H/D)

Fig. 8. Effects of FRP fabric type coupled with other parameters on (f_{cc}) of confined specimens.

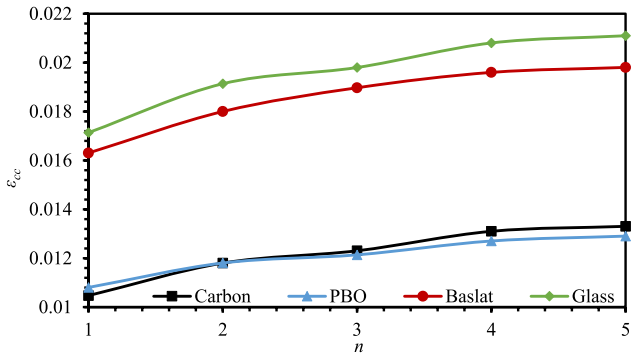

(a) Number of FRP fabric layers (n)

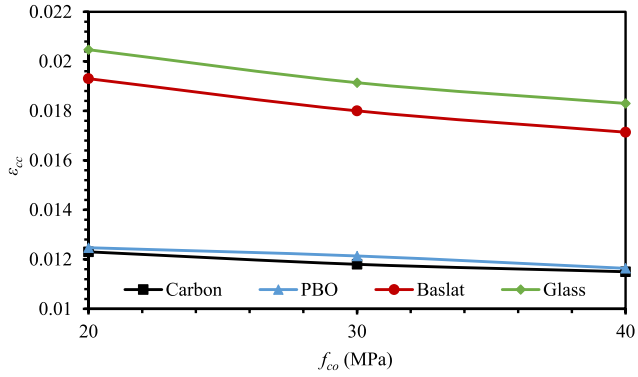

(b) Compressive strength of unconfined concrete (f_{co})

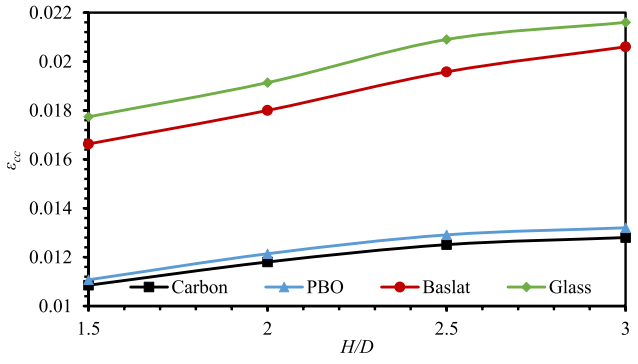

(c) Height/diameter ratio (H/D)

Fig. 9. Effects of FRP fabric type coupled with other parameters on (ε_{cc}) of confined specimens.

magnitude for the fabric elastic modulus in Table 3. Similar trend, but noticeably more linear, can also be seen in Fig. 8(b) when plotting f_{cc} against f_{co} for all fabric types. For PBP-FRCM confined concrete cylinders, f_{cc} increased by 28% when f_{co} is increased from 20 to 40 MPa. Also, like what was observed earlier, Fig. 8(c) shows that f_{cc} is not affected by H/D ratio, for any of the fabrics.

The comparison of peak axial strain (ε_{cc}) for different types of fabrics, in conjunction with various values for n, f_{co}, and (H/D) ratio, is presented in Fig. 9. It can be noticed in this figure that GFRCM results in a better axial straining than other fabric types, followed by BFRCM, PBO-FRCM, and CFRCM. The strain behavior of the four considered fabrics is proportional to FRP elastic modulus (E_f) as listed in Table 3. Similar conclusion was also reached in the study by Di Ludovico, et al. [26]. Fig. 9 shows, for all fabric types, that ε_{cc} increases with n and (H/D) ratio and decreases with f_{co}.

7. Evaluation of existing confinement models

Predictions of f_{cc} and ε_{cc} from the two best performing FRCM confinement models identified earlier (Ombres and Mazzuca [27]) and ACI 549 [12]) were compared with FE results in Figs. 10 and 11, respectively. The goal is to investigate the sensitivity of existing models to two parameters, mortar compressive strength (f_m) and thickness (t_m), found to have a significant effect on the behavior of FRCM-confined concrete as demonstrated earlier. Mechanical properties of the confined cylinder used in the numerical and analytical comparisons are the same as before, except with varying f_m and t_m.

Because the two models do not explicitly include the effects of mortar properties, their predictions were insensitive to the variation of f_m and t_m, unlike the FE model which clearly shows the impact of these parameters in Figs. 10 and 11. It is therefore of great value to develop a new model capable of capturing these variables. Figs. 10 and 11 also plot the predictions of the new model developed in this paper and discussed in the next section, showing its ability to capture the effects of mortar

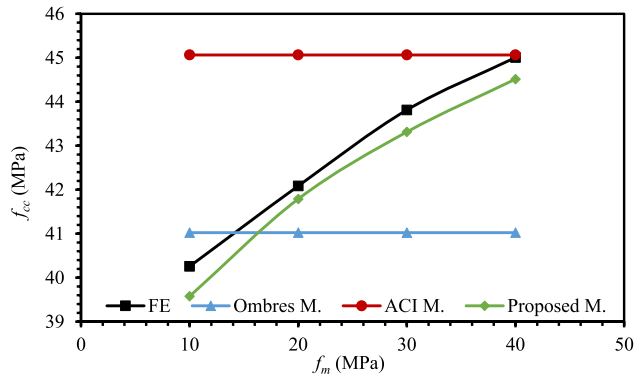

(a) Against mortar compressive strength (f_m)

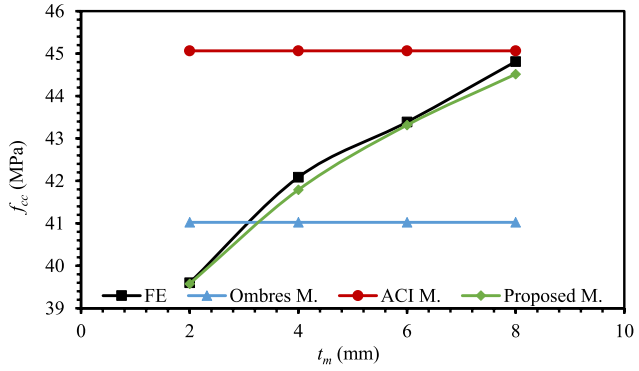

(b) Against mortar thickness (t_m)

Fig. 10. Performance of proposed and existing confinement models vs. FE predictions of f_{cc} considering effects of mortar properties (f_m, t_m).

properties on the peak compressive strength and accompanying strains of FRCM-confined concrete.

8. Proposed model

In this section, a design-oriented confinement model is developed for FRCM-confined concrete, using an experimental database of 139 specimens reported in literature [1–4,7,26,29,30,48–50], augmented by 144 FE models developed in this study, totaling 283 data points. Table 4 lists the experimental specimens collected from the literature and their geometric and mechanical properties. The database includes articles published from 2006 to 2019, involving various specimen properties with the following ranges: f_{co} from 15 to 29 MPa, n from 1 to 4, D from 113 to 200 mm, and E_f from 52 to 270 GPa, corresponding to the four different types of FRP fabrics discussed in this study.

The confined-to-unconfined concrete strengths (f_{cc}/f_{co}) and strains ($\varepsilon_{cc}/\varepsilon_{co}$) predicted using the two existing confinement models are compared with the FE parametric cases in Fig. 12. The comparison is used to assess the performance of the two existing models and select the best one to be modified to include the effects of mortar properties. It can be seen from Fig. 12 that both models were able to reasonably predict f_{cc} with a good level of accuracy, where the mean values of (f_{cc}/f_{co}) and MSE are 1.27 and 0.009 for Ombres and Mazzuca and 1.32 and 0.025 for ACI 549. MSE is the mean square error which can be calculated using Eq. (11):

$$MSE = \frac{1}{N}\sum_{i=1}^{n}\left[\frac{f_{ccFE}}{f_{co}} - \frac{f_{ccth}}{f_{co}}\right]_i^2 \tag{11}$$

where N is the number of specimens and f_{ccFE} and f_{ccth} represent the finite element and theoretical strength capacities of confined concrete

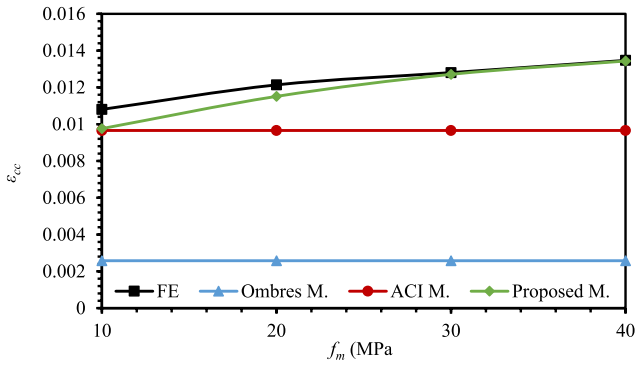

(a) Against mortar compressive strength (f_m)

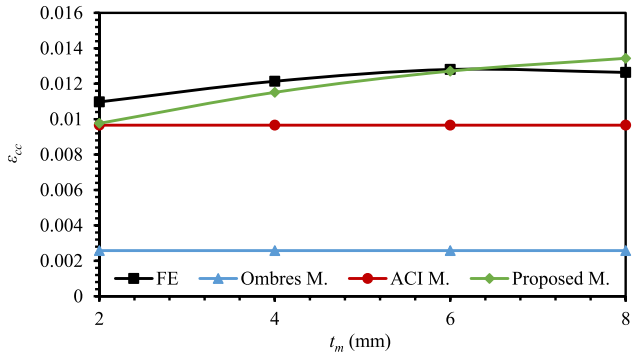

(b) Against mortar thickness (t_m)

Fig. 11. Performance of proposed and existing confinement models vs. FE predictions of ε_{cc} considering effects of mortar properties (f_m, t_m).

specimens.

The mean and MSE values indicate that the variation from the Ombres and Mazzuca model is less than that from the ACI model. Similar conclusion can be drawn from the comparisons of (f_{cc}/f_{co}) obtained from experimental tests and predictions of the two existing confinement models as seen in Fig. 13; where the mean and MSE values are 1.33 and 0.098 for Ombres and Mazzuca and 1.55 and 0.182 for ACI 549. The comparisons of ($\varepsilon_{cc}/\varepsilon_{co}$) from the FE models and experimental tests also point to the same conclusion. Therefore, the Ombres and Mazzuca model is selected to include the effects of mortar properties and to improve its predictions of the peak strain value (ε_{cc}).

A new non-dimensional parameter (k_m) is introduced to account for the effects of mortar properties, calculated from fitting the 283 experimental and numerical data as follows:

$$k_m = \alpha_m\left(\frac{4nf_mt_m}{f_{co}D}\right)^{\beta_m} \tag{12}$$

Then, the peak compressive strength of confined concrete (f_{cc}) is calculated from Ombres and Mazzuca model (Eq. (5)) with the added k_m coefficient as:

$$\frac{f_{cc}}{f_{co}} = 1 + 0.913k_m\left(\frac{f_{lu}}{f_{co}}\right)^{0.5} \tag{13}$$

where α_m and β_m are unknown parameters representing the effects of mortar properties, to be calibrated through statistical fitting. Best-fit analysis was performed as shown in Fig. 14 where the term $[(f_{cc} - f_{co})_{FE}/(f_{cc} - f_{co})_{th}]$, which is selected because it refers to the pure contribution of FRCM system to concrete strength, is plotted against the variable ($4n\ f_m\ t_m/f_{co}\ D$) encompassing the mortar mechanical properties. The subscripts (FE) and (th) refer to finite element and theoretical predictions from Ombres and Mazzuca model, respectively. Based on the

Table 4
Properties of FRCM-confined cylindrical specimens from literature.

#	f_{co} (MPa)	ε_{co} (%)	θ	t_f (mm)	E_f (GPa)	D (mm)	n	tm (mm)	fm(MPa)	f_{cc} (MPa)	ε_{cc} (%)	Ref
S1	15.4	0.37	90	0.0455	270.0	152	1	6	30.4	24.69	1.15	[3]
S2	15.4	0.37	90	0.0455	270.0	152	2	9	30.4	35.00	2.00	
S3	15.4	0.37	90	0.0455	270.0	152	3	12	30.4	41.45	2.90	
S4	15.4	0.37	90	0.0455	270.0	152	4	15	30.4	49.24	2.64	
S5	15.4	0.37	45	0.0455	270.0	152	1	6	30.4	16.19	1.36	
S6	15.4	0.37	45	0.0455	270.0	152	2	9	30.4	16.98	2.10	
S7	15.4	0.37	45	0.0455	270.0	152	3	12	30.4	17.40	3.14	
S8	15.4	0.37	30	0.0455	270.0	152	2	9	30.4	17.45	2.44	
S9	15.4	0.37	30	0.0455	270.0	152	3	12	30.4	21.69	2.32	
S10	29.3	0.74	90	0.0455	270.0	153	1	6	30.4	43.55	0.80	
S11	29.3	0.74	90	0.0455	270.0	153	2	9	30.4	47.00	1.48	
S12	29.3	0.74	90	0.0455	270.0	153	3	12	30.4	56.60	1.93	
S13	29.3	0.74	90	0.0455	270.0	153	4	15	30.4	56.23	2.16	
S14	29.3	0.74	45	0.0455	270.0	152	1	6	30.4	31.68	0.67	
S15	29.3	0.74	45	0.0455	270.0	152	2	9	30.4	33.79	0.81	
S16	29.3	0.74	45	0.0455	270.0	152	3	12	30.4	35.72	0.88	
S17	29.3	0.74	30	0.0455	270.0	152	2	9	30.4	35.42	0.96	
S18	29.3	0.74	30	0.0455	270.0	152	3	12	30.4	39.52	1.11	
S19	58.1	0.54	90	0.0455	270.0	150	1	6	30.4	54.90	0.56	
S20	58.1	0.54	90	0.0455	270.0	150	2	9	30.4	51.45	0.63	
S21	58.1	0.54	90	0.0455	270.0	150	3	12	30.4	55.94	0.52	
S22	19.5	0.27	90	0.0455	240.0	150	2	6*	30.4*	29.63	0.53	[48]
S23	19.5	0.27	90	0.0455	240.0	150	2	6	30.4	28.33	0.56	
S24	19.5	0.27	90	0.0455	240.0	150	2	6	30.4	22.67	0.70	
S25	19.5	0.27	90	0.0455	240.0	150	3	9	30.4	30.56	0.63	
S26	19.5	0.27	90	0.0455	240.0	150	3	9	30.4	30.84	1.42	
S27	19.5	0.27	90	0.0455	240.0	150	3	9	30.4	32.86	1.21	
S28	19.5	0.27	90	0.0455	240.0	150	4	12	30.4	33.17	1.21	
S29	19.5	0.27	90	0.0455	240.0	150	4	12	30.4	35.10	1.31	
S30	19.5	0.27	90	0.0455	240.0	150	4	12	30.4	36.96	1.68	
S31	24.2	0.13	90	0.0455	270.0	154	2	9	15	30.60	1.16	[29]
S32	24.2	0.13	90	0.0455	270.0	154	2	9	15	31.30	0.68	
S33	24.2	0.13	90	0.0455	270.0	154	2	9	15	31.80	0.31	
S34	24.2	0.13	90	0.0455	270.0	154	3	12	15	33.80	0.96	
S35	24.2	0.13	90	0.0455	270.0	154	3	12	15	36.20	1.14	
S36	24.2	0.13	90	0.0455	270.0	154	3	12	15	39.70	1.49	
S37	24.4	0.19	90	0.0455	270.0	200	2	9	15	30.80	0.22	
S38	24.4	0.19	90	0.0455	270.0	200	2	9	15	33.70	1.27	
S39	24.4	0.19	90	0.0455	270.0	200	2	9	15	29.00	0.17	
S40	24.4	0.19	90	0.0455	270.0	200	3	12	15	34.70	0.92	
S41	24.4	0.19	90	0.0455	270.0	200	3	12	15	32.40	0.24	
S42	22.6	0.25	90	0.0455	270.0	113	1	8	16.0	32.48	0.62	[30]
S43	22.6	0.25	90	0.0455	270.0	113	1	8	16.0	32.66	0.70	
S44	22.6	0.25	90	0.0455	270.0	113	2	12	16.0	42.48	1.21	
S45	22.6	0.25	90	0.0455	270.0	113	2	12	16.0	42.96	1.14	
S46	22.6	0.25	90	0.0455	270.0	113	3	16	16.0	58.07	1.81	
S47	22.6	0.25	90	0.0455	270.0	113	3	16	16.0	55.80	1.71	
#	f_{co} (MPa)	ε_{co} (%)	θ	t_f (mm)	E_f (GPa)	D (mm)	n	tm (mm)	fm(MPa)	f_{cc} (MPa)	ε_{cc} (%)	Ref
S48	20.4	0.24	90	0.2460	72.4	152	2	9	2.5	29.40	0.95	[1]
S49	20.4	0.24	90	0.2460	72.4	152	2	9	2.5	24.30	0.85	
S50	20.4	0.24	90	0.2460	72.4	152	2	9	31.1	30.00	0.83	
S51	20.4	0.24	90	0.2460	72.4	152	2	9	31.1	30.00	0.75	
S52	21.7	0.25	90	0.2460	72.4	152	1	6	31.1	26.80	0.33	
S53	21.7	0.25	90	0.2460	72.4	152	1	6	31.1	24.50	0.33	
S54	21.7	0.25	90	0.2460	72.4	152	1	6	31.1	27.60	0.36	
S55	21.7	0.25	90	0.2460	72.4	152	2	9	31.1	33.10	1.15	
S56	21.7	0.25	90	0.2460	72.4	152	2	9	31.1	36.90	0.86	
S57	21.7	0.25	90	0.2460	72.4	152	2	9	31.1	33.00	1.44	
S58	21.7	0.25	90	0.2460	72.4	152	2	9	31.1	32.30	0.89	
S59	21.7	0.25	90	0.2460	72.4	152	2	9	31.1	40.40	1.10	
S60	21.7	0.25	90	0.2460	72.4	152	2	9	31.1	37.40	1.17	
S61	21.7	0.25	90	0.2460	72.4	152	2	9	31.1	35.00	0.40	
S62	21.7	0.25	90	0.2460	72.4	152	2	9	31.1	33.10	0.37	
S63	21.7	0.25	90	0.2460	72.4	152	2	9	31.1	31.50	0.60	
S64	21.7	0.25	90	0.2460	72.4	152	2	9	31.1	39.20	0.96	
S65	21.7	0.25	90	0.2460	72.4	152	2	9	31.1	34.10	0.92	
S66	21.7	0.25	90	0.2460	72.4	152	2	9	31.1	30.70	0.54	
S67	21.7	0.25	90	0.2460	72.4	152	4	15	31.1	48.60	0.98	
S68	21.7	0.25	90	0.2460	72.4	152	4	15	31.1	47.90	0.98	
S69	21.7	0.25	90	0.2460	72.4	152	4	15	31.1	47.10	0.98	
S70	15.5	0.23	90	0.0460	91.1	150	2	12	30.0	22.35	0.32	[26]
S71	17.8	0.29	90	0.0460	91.1	150	1	8	30.0	18.01	0.44	
S72	17.8	0.29	90	0.0460	91.1	150	1	8	30.0	20.15	0.26	

(*continued on next page*)

Table 4 (*continued*)

#	f_{co} (MPa)	ε_{co} (%)	θ	t_f (mm)	E_f (GPa)	D (mm)	n	tm (mm)	fm(MPa)	f_{cc} (MPa)	ε_{cc} (%)	Ref
S73	17.8	0.29	90	0.0460	91.1	150	1	8	30.0	21.93	0.47	
S74	17.8	0.29	90	0.0460	91.1	150	2	12	30.0	23.00	0.52	
S75	15.5	0.23	90	0.0460	91.1	150	1	8	30.0	22.50	0.55	
S76	15.5	0.23	90	0.0460	91.1	150	2	12	30.0	22.81	0.62	
S77	17.8	0.29	90	0.0460	91.1	150	1	8	30.0	24.07	0.39	
S78	17.8	0.29	90	0.0460	91.1	150	1	8	30.0	26.57	0.44	
S79	17.8	0.29	90	0.0460	91.1	150	2	12	30.0	28.71	0.65	
S80	17.8	0.29	90	0.0460	91.1	150	2	12	30.0	27.99	0.37	
S81	15.5	0.23	90	0.0460	91.1	150	1	8	30.0	19.71	0.27	
S82	15.5	0.23	90	0.0460	91.1	150	2	12	30.0	22.50	0.71	
S83	17.8	0.29	90	0.0460	91.1	150	1	8	30.0	26.39	0.34	
S84	17.8	0.29	90	0.0460	91.1	150	1	8	30.0	19.43	0.27	
S85	17.8	0.29	90	0.0460	91.1	150	2	12	30.0	27.64	0.57	
S86	17.8	0.29	90	0.0460	91.1	150	2	12	30.0	25.85	0.71	
S87	22.5	0.11	90	0.0455	270.0	300	1	6	16.1	30.33	0.17	[49]
S88	22.5	0.11	90	0.0455	270.0	300	2	9	16.1	31.33	0.24	
S89	22.5	0.11	90	0.0455	270.0	300	4	15	16.1	32.50	0.39	
S90	15.2	0.20	90	0.0455	225.0	150	2	6	8.7	20.77	0.96	[4]
S91	15.2	0.20	90	0.0455	225.0	150	2	6	30.6	23.88	1.08	
S92	15.2	0.20	90	0.0455	225.0	150	3	8	8.7	26.50	1.13	
S93	15.2	0.20	90	0.0455	225.0	150	3	8	30.6	27.00	1.22	
S94	21.8	0.20	90	0.0455	225.0	150	2	6	30.6	27.36	0.98	
S95	21.8	0.20	90	0.0455	225.0	150	3	8	30.6	32.44	1.08	
S96	21.8	0.41	90	0.0865	52.0	150	1	10	22.4	25.51	0.51	[7]
S97	21.8	0.41	90	0.0865	52.0	150	1	10	22.4	25.94	0.55	
S98	21.8	0.41	90	0.0865	52.0	150	1	10	22.4	27.47	0.53	
S99	21.8	0.41	90	0.0865	52.0	150	1	10	22.4	27.03	0.55	
S100	21.8	0.41	90	0.0865	52.0	150	1	10	22.4	24.42	0.55	
S101	21.8	0.41	90	0.0865	52.0	150	1	10	22.4	26.81	0.61	
S102	21.8	0.41	90	0.0865	52.0	150	2	15	22.4	29.21	0.59	[7]
S103	21.8	0.41	90	0.0865	52.0	150	2	15	22.4	27.90	0.57	
S104	21.8	0.41	90	0.0865	52.0	150	2	15	22.4	26.38	0.62	
S105	21.8	0.41	90	0.0865	52.0	150	2	15	22.4	24.85	0.50	
S106	21.8	0.41	90	0.0865	52.0	150	2	15	22.4	27.25	0.57	
S107	21.8	0.41	90	0.0865	52.0	150	2	15	22.4	27.69	0.57	
S108	15.1	0.24	90	0.5840	130.2	150	1	8	22.1	21.29	0.47	[50]
S109	15.1	0.24	90	0.5840	130.2	150	1	8	22.1	23.24	0.52	
S110	15.1	0.24	90	0.1240	130.2	150	1	8	22.1	26.73	0.83	
S111	15.1	0.24	90	0.1240	130.2	150	1	8	22.1	22.67	0.33	
S112	15.1	0.24	90	0.1240	130.2	150	1	8	22.1	27.58	0.88	
S113	15.1	0.24	90	0.0620	130.2	150	1	8	22.1	22.35	0.55	
S114	15.1	0.24	90	0.0620	130.2	150	1	8	22.1	23.10	0.44	
S115	15.1	0.24	90	0.0620	130.2	150	1	8	22.1	22.94	0.58	
S116	15.1	0.24	90	0.5840	130.2	150	1	8	22.1	24.18	0.41	
S117	15.1	0.24	90	0.5840	130.2	150	1	8	22.1	26.41	0.44	
S118	15.1	0.24	90	0.1240	130.2	150	1	8	22.1	24.84	0.58	
S119	15.1	0.24	90	0.1240	130.2	150	1	8	22.1	27.46	0.62	
S120	15.1	0.24	90	0.1240	130.2	150	1	8	22.1	27.63	0.77	
S121	15.1	0.24	90	0.0620	130.2	150	1	8	22.1	20.94	0.37	
S122	15.1	0.24	90	0.0620	130.2	150	1	8	22.1	21.95	0.34	
S123	15.1	0.24	90	0.0620	130.2	150	1	8	22.1	24.77	0.37	
S124	26.2	0.25	90	0.1240	130.2	150	1	8	22.1	31.47	0.31	
S125	26.2	0.25	90	0.1240	130.2	150	1	8	22.1	34.17	0.31	
S126	26.2	0.25	90	0.1240	130.2	150	1	8	22.1	42.57	0.33	
S127	26.2	0.25	90	0.0620	130.2	150	1	8	22.1	34.08	0.27	
S128	26.2	0.25	90	0.0620	130.2	150	1	8	22.1	37.86	0.31	
S129	26.2	0.25	90	0.0620	130.2	150	1	8	22.1	35.84	0.28	
S130	26.2	0.25	90	0.1240	130.2	150	1	8	22.1	42.99	0.41	
S131	26.2	0.25	90	0.1240	130.2	150	1	8	22.1	40.83	0.30	
S132	26.2	0.25	90	0.1240	130.2	150	1	8	22.1	37.43	0.42	
S133	26.2	0.25	90	0.0620	130.2	150	1	8	22.1	36.78	0.26	
S134	26.2	0.25	90	0.0620	130.2	150	1	8	22.1	37.90	0.29	
S135	26.2	0.25	90	0.0620	130.2	150	1	8	22.1	33.95	0.28	
S136	17.9	0.20	90	0.0470	242.0	100	2	12	22.9	19.20	0.13	[2]
S137	16.8	0.16	90	0.0470	242.0	154	2	12	22.9	22.40	0.33	
S138	16.8	0.16	90	0.0470	242.0	154	2	12	22.9	19.50	0.18	
S139	16.8	0.16	90	0.0470	242.0	154	2	12	22.9	16.60	0.25	

f_{co} and ε_{co} compressive strength of unconfined concrete and the corresponding axial strain respectively; θ = angle of inclination of fibres with respect to the longitudinal axis; t_f = equivalent fibers thickness; E_f = fibers elastic modulus; D = diameter of specimens; n = number of the fabric meshes; t_m: mortar thickness; f_m = compressive strength of mortar and f_{cc} and ε_{cc} = peak compressive strength of confined concrete and the corresponding axial strain respectively.
(*) values of t_m and f_m were assumed since they were not given in the study.

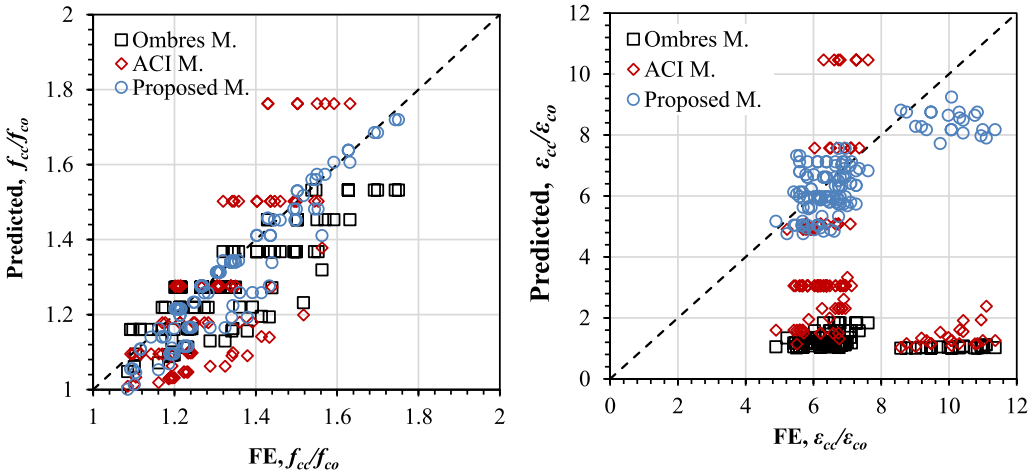

Ombres M. (MSE =0.009, Mean=1.27)
ACI M. (MSE =0.025, Mean=1.32)
Proposed M. (MSE=0.003, Mean=1.29)
FE (Mean= 1.32)

Ombres M. (MSE =35.09, Mean=1.22)
ACI M. (MSE =21.40, Mean=3.51)
Proposed M. (MSE=1.06, Mean=6.49)
FE (Mean= 6.93)

Fig. 12. Comparisons of (f_{cc}/f_{co}) and ($\varepsilon_{cc}/\varepsilon_{co}$), from FE model results and predictions of existing and proposed confinement models.

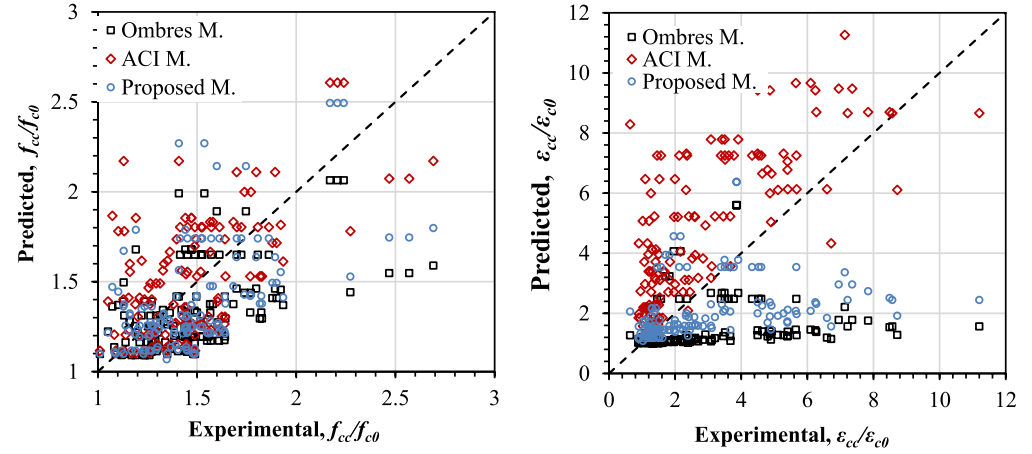

Ombres M. (MSE =0.101, Mean=1.33)
ACI M. (MSE=0.186, Mean=1.55)
Proposed M. (MSE=0.090, Mean=1.38)
Experimental (Mean= 1.45)

Ombres M. (MSE =6.02, Mean=1.49)
ACI M. (MSE =18.25, Mean=5.44)
Proposed M. (MSE=4.43, Mean=2.04)
Experimental (Mean= 2.86)

Fig. 13. Comparisons of (f_{cc}/f_{co}) and ($\varepsilon_{cc}/\varepsilon_{c0}$), from experimental results and predictions of existing and proposed confinement models.

best-fit analysis, α_m and β_m were found to be 1.7 and 0.3, respectively, and the R^2 values was 0.89 indicating a good statistical fit. Therefore, Eq. (12) can be rearranged as:

$$k_m = 1.7\left(\frac{4nf_m t_m}{f_{c0}D}\right)^{0.3} \tag{14}$$

A predictive equation can also be found for the peak axial strain (ε_{cc}) by using Ombress and Mazzuca model for strain (Eq. (6)), introducing the same non-dimensional parameter (k_m) and minimizing the average percentage error (APE_ε) as follows:

$$APE_\varepsilon = \frac{1}{n}\sum_{i=1}^{n}\frac{\left(\frac{\varepsilon_{cc}}{\varepsilon_{co}}\right)_{th} - \left(\frac{\varepsilon_{cc}}{\varepsilon_{co}}\right)_{FE}}{\left(\frac{\varepsilon_{cc}}{\varepsilon_{co}}\right)_{FE}} \tag{15}$$

Consequently, ε_{cc} can be rearranged in Eq.16, after minimizing APE_ε to 0.008 from an initial un-conservative value of 0.816 in the original Ombres and Mazzuca model:

$$\frac{\varepsilon_{cc}}{\varepsilon_{co}} = 1 + 0.963k_m\left(\frac{f_{lu}}{f_{co}}\right)^{0.4}\left(\frac{\varepsilon_{fe}}{\varepsilon_{co}}\right)^{0.5} \tag{16}$$

Fig. 12 compares the model predictions and FE results of (f_{cc}/f_{co}) and ($\varepsilon_{cc}/\varepsilon_{co}$). The figure shows that the model has lower MSE values of 0.003 and 1.06 for predictions of f_{cc} and ε_{cc}, respectively, compared to the respective values of 0.009 and 35.09 from Ombres and Mazzuca model. Also, Fig. 13 compares the model to the experimental results and shows a mean and MSE values of 1.38 and 0.09, respectively, compared to 1.33 and 0.101 from Ombres and Mazzuca model. The mean of the proposed model for (f_{cc}/f_{co}) is much closer to the experimentally found mean of 1.45. In addition, the same conclusions can be drawn for ($\varepsilon_{cc}/\varepsilon_{co}$) in

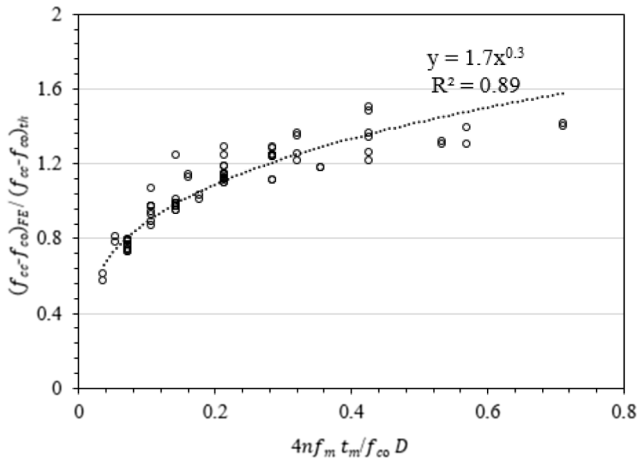

Fig. 14. Best-fit analysis and relation between ($4n\ f_m\ t_m/\ f_{co}\ D$) and [$(f_{cc} - f_{co})_{FE}/(f_{cc} - f_{co})_{th}$].

Fig. 13, with a mean and MSE values of 2.04 and 4.43, respectively, compared to 1.49 and 6.02 from Ombres and Mazzuca model. The mean of the proposed model for ($\varepsilon_{cc}/\varepsilon_{co}$) is much closer to the experimentally found mean of 2.86. In conclusion, the proposed model provided closer predictions to experimental results than existing models for both, the peak strength and peak strain estimations. However, the model still needs further improvements to address the large deviations for predictions of peak strain (ε_{cc}), evidenced by the large MSE of 4.43 for peak strain compared to only 0.09 MSE for peak stress (f_{cc}) (Fig. 13). The deviation in strain predictions is attributed to the large scatter and inconsistency of reported failure strains from experimental tests.

It can be concluded that the proposed model performs better than the existing models (Ombres and Mazzuca and ACI-549), likely because it was derived from a larger specimen database and incorporates the effects of mortar properties (f_m and t_m) that are absent in other models, thus resulting in better predictions as can be seen in Figs. 10 to 13. The proposed model can be implemented within any design codes such as ACI 549 [28] guide, where f_{cc} and ε_{cc} are typically used in calculating the capacity of confined column. Further details and guidance about designing FRCM-confined axial members along with design examples can be found in [28].

9. Conclusions and recommendations

In this study, the behavior of concrete confined by fiber-reinforced cementitious mortar (FRCM) jackets has been studied, with the aim of developing an improved design-oriented confinement model for the system. The few existing confinement models for this system were discussed and the best performing one was identified. It was later modified to consider the effects of mortar properties and provide better statistical performance.

A large experimental database comprising 139 specimens with various geometrical and material properties was developed from literature and carefully analyzed to identify behavioral aspects, limitations, and research gaps. A robust, three-dimensional finite element (FE) model was developed for the FRCM-confined concrete specimens and verified with test results of 33 experiments, covering a wide range of examined variables and confinement levels. The FE model predictions for peak strength, general stress–strain behavior, and failure modes matched well those from testing. The FE model was then used to carry out a comprehensive parametric analysis, resulting in 144 additional numerical specimens, and a total of 283 experimental and numerical data points combined.

The parameters investigated numerically were: compressive strength of mortar (f_m), varying f_m from 10 to 40 MPa; thickness of mortar layer (t_m); type of FRP fabric, examining four types, Benzobis Oxazole (PBO-FRCM), Carbon (C-FRCM), Glass (G-FRCM), and Basalt (B-FRCM); number of FRCM layers (n), varying n from 1 to 5; compressive strength of unconfined concrete (f_{co}), utilizing three values for f_{co}, 20, 30 and 40 MPa; and height-to-diameter ratio (H/D) for cylindrical specimens, examining three values, 1.5, 2, 2.5, and 3. The results showed that the confined concrete strength (f_{cc}) increases linearly as the mortar compressive strength and thickness increase, for all examined n, f_{co}, and (H/D) values. f_{cc} also varies almost linearly with n for all fabric types. PBO-FRCM system is more effective than other fabric types, followed by CFRCM, BFRCM, and GFRCM.

In addition to augmenting the database for stronger statistical analysis and model development, the parametric analysis also focused on better understanding the effects of mortar properties, namely: its compressive strength (f_m) and thickness (t_m), which were neglected in all existing confinement models. A noticeable increase of peak strength (f_{cc}) of confined concrete, was observed in the FE analysis when either f_m or t_m are increased.

The proposed confinement model, derived from regression analysis and minimization of the average percentage error, comprised semi-empirical formulations for the peak strength (f_{cc}) and accompanying strain (ε_{cc}) of confined concrete, including a coefficient for the effects of f_m and t_m. It provided much better statistical performance and correlation with results from experimental tests and numerical simulations, than existing confinement models.

CRediT authorship contribution statement

Ali Hadi Adheem: Investigation, Validation, Writing – original draft, Writing – review & editing, Visualization. **Majid M.A. Kadhim:** Conceptualization, Methodology, Investigation, Visualization, Writing – original draft, Writing – review & editing. **Akram Jawdhari:** Conceptualization, Methodology, Investigation, Validation, Formal analysis, Writing – original draft, Writing – review & editing. **Amir Fam:** Conceptualization, Methodology, Writing – review & editing, Visualization.

Declaration of Competing Interest

The authors declare that they have no known competing financial interests or personal relationships that could have appeared to influence the work reported in this paper.

References

[1] F.J. De Caso y Basalo, F. Matta, A. Nanni, Fiber reinforced cement-based composite system for concrete confinement, Constr. Build. Mater. 32 (2012) 55–65.
[2] J. Gonzalez-Libreros, M.A. Zanini, F. Faleschini, C. Pellegrino, Confinement of low-strength concrete with fiber reinforced cementitious matrix (FRCM) composites, Composites Part B: Engineering 177 (2019), 107407.
[3] L. Ombres, Concrete confinement with a cement based high strength composite material, Compos. Struct. 109 (2014) 294–304.
[4] T.C. Triantafillou, C.G. Papanicolaou, P. Zissimopoulos, T. Laourdekis, Concrete confinement with textile-reinforced mortar jackets, ACI Mater. J. 103 (1) (2006) 28.
[5] A. Jawdhari, A.H. Adheem, M.M. Kadhim, Parametric 3D finite element analysis of FRCM-confined RC columns under eccentric loading, Eng. Struct. 212 (2020), 110504.
[6] A. Jawdhari, A. Fam, I. Harik, Bond between CFRP rod panels and concrete using cementitious mortar, Constr. Build. Mater. 235 (2020), 117503.
[7] D. García, P. Alonso, J.-T. San-José, L. Garmendia, C. Perlot, Confinement of medium strength concrete cylinders with basalt Textile Reinforced Mortar. in *ICPIC 2010–13th International Congress on Polymers in Concrete*, 2010.
[8] F. Faleschini, M.A. Zanini, L. Hofer, C. Pellegrino, Experimental behavior of reinforced concrete columns confined with carbon-FRCM composites, Constr. Build. Mater. 243 (2020), 118296.
[9] Sabau, C., *FRCM-Composites for Strengthening Concrete Walls with Openings: Experimental and Numerical Analysis*, 2018, Luleå University of Technology.
[10] Koutas, L.N., Tetta, Z., Bournas, D.A. and Triantafillou, T.C., *Strengthening of concrete structures with textile reinforced mortars: state-of-the-art review*, 2019, American Society of Civil Engineers.

[11] L.H. Sneed, S. Verre, C. Carloni, L. Ombres, Flexural behavior of RC beams strengthened with steel-FRCM composite, Eng. Struct. 127 (2016) 686–699.
[12] G. Loreto, L. Leardini, D. Arboleda, A. Nanni, Performance of RC slab-type elements strengthened with fabric-reinforced cementitious-matrix composites, J. Compos. Constr. 18 (3) (2014) A4013003.
[13] Z.C. Tetta, L.N. Koutas, D.A. Bournas, Textile-reinforced mortar (TRM) versus fiber-reinforced polymers (FRP) in shear strengthening of concrete beams, Compos. B Eng. 77 (2015) 338–348.
[14] M.Y. Alabdulhady, L.H. Sneed, C. Carloni, Torsional behavior of RC beams strengthened with PBO-FRCM composite–an experimental study, Eng. Struct. 136 (2017) 393–405.
[15] C.G. Papanicolaou, T.C. Triantafillou, M. Papathanasiou, K. Karlos, Textile reinforced mortar (TRM) versus FRP as strengthening material of URM walls: out-of-plane cyclic loading, Mater. Struct. 41 (1) (2007) 143–157.
[16] S. Babaeidarabad, A. Nanni, Out-of-plane strengthening of URM walls with Fabric-Reinforced-Cementitious-Matrix (FRCM), Special Publication 299 (2015) 1–12.
[17] D.A. Bournas, P.V. Lontou, C.G. Papanicolaou, T.C. Triantafillou, Textile-reinforced mortar versus fiber-reinforced polymer confinement in reinforced concrete columns, ACI Struct. J. 104 (6) (2007) 740.
[18] T. Trapko, Behaviour of fibre reinforced cementitious matrix strengthened concrete columns under eccentric compression loading, Mater. Des. 54 (2014) 947–954.
[19] L. Ombres, S. Verre, Structural behaviour of fabric reinforced cementitious matrix (FRCM) strengthened concrete columns under eccentric loading, Compos. B Eng. 75 (2015) 235–249.
[20] G.C.Z.T.D.B. Bournas L. Concrete confinement with TRM versus FRP jackets at elevated temperatures Materials and Structures 53 2020 58.
[21] R. Feng, Y. Li, J.-H. Zhu, F. Xing, Behavior of corroded circular RC columns strengthened by C-FRCM under cyclic loading, Eng. Struct. 226 (2021), 111311.
[22] K. Toska, F. Faleschini, FRCM-confined concrete: Monotonic vs, *Cyclic axial loading.* Composite Structures 268 (2021), 113931.
[23] T. Trapko, K. Rogalski, M. Musiał, L. Ombres, Effectiveness of Concrete Elements Strengthening through PBO-FRCM Confinement with Various Types of Anchorage, J. Mater. Civ. Eng. 33 (1) (2021) 04020409, https://doi.org/10.1061/(ASCE)MT.1943-5533.0003510.
[24] K. Toska, F. Faleschini, M.A. Zanini, L. Hofer, C. Pellegrino, Repair of severely damaged RC columns through FRCM composites, Constr. Build. Mater. 273 (2021), 121739.
[25] P. Yoddumrong, K. Rodsin, S. Katawaethwarag, Seismic strengthening of low-strength RC concrete columns using low-cost glass fiber reinforced polymers (GFRPs), Case Stud. Constr. Mater. 13 (2020) e00383, https://doi.org/10.1016/j.cscm.2020.e00383.
[26] M. Di Ludovico, A. Prota, G. Manfredi, Structural upgrade using basalt fibers for concrete confinement, J. Compos. Constr. 14 (5) (2010) 541–552.
[27] L. Ombres, S. Mazzuca, Confined concrete elements with cement-based composites: confinement effectiveness and prediction models, J. Compos. Constr. 21 (3) (2017) 04016103, https://doi.org/10.1061/(ASCE)CC.1943-5614.0000755.
[28] ACI, *Guide to design and construction of externally bonded fabric-reinforced cementitious matrix (FRCM) systems for repair and strengthening concrete and masonry structures*, 2013, Farmington Hills MI, USA.
[29] P. Colajanni, F. De Domenico, A. Recupero, N. Spinella, Concrete columns confined with fibre reinforced cementitious mortars: experimentation and modelling, Constr. Build. Mater. 52 (2014) 375–384.
[30] T. Trapko, Confined concrete elements with PBO-FRCM composites, Constr. Build. Mater. 73 (2014) 332–338.
[31] ANSYS, *Release 17.2 Documentation for ANSYS.* Version 17.2, ANSYS Inc., Canonsburg, PA, USA, 2016.
[32] A. Jawdhari, I. Harik, Finite element analysis of RC beams strengthened in flexure with CFRP rod panels, Constr. Build. Mater. 163 (2018) 751–766.
[33] S. Verre, L. Ombres, Numerical modelling approaches of FRCMs/SRG confined masonry columns, Frontiers in Built Environment 5 (2019) 143.
[34] H.M. Elsanadedy, Y.A. Al-Salloum, S.H. Alsayed, R.A. Iqbal, Experimental and numerical investigation of size effects in FRP-wrapped concrete columns, Constr. Build. Mater. 29 (2012) 56–72.
[35] J.-K. Son, A. Fam, Finite element modeling of hollow and concrete-filled fiber composite tubes in flexure: Model development, verification and investigation of tube parameters, Eng. Struct. 30 (10) (2008) 2656–2666.
[36] A. Mirmiran, K. Zagers, W. Yuan, Nonlinear finite element modeling of concrete confined by fiber composites, Finite Elem. Anal. Des. 35 (1) (2000) 79–96.
[37] L. Lam, J.G. Teng, Design-oriented stress–strain model for FRP-confined concrete, Constr. Build. Mater. 17 (6-7) (2003) 471–489.
[38] C.E. Bakis, A. Ganjehlou, D.I. Kachlakev, M. Schupack, P. Balaguru, D.J. Gee, V. M. Karbhari, D.W. Scott, C.A. Ballinger, T.R. Gentry, Guide for the design and construction of externally bonded FRP systems for strengthening concrete structures, Reported by ACI Committee 440 (2002) (2002).
[39] A. Fam, J.-K. Son, Finite element modeling of hollow and concrete-filled fiber composite tubes in flexure: Optimization of partial filling and a design method for poles, Eng. Struct. 30 (10) (2008) 2667–2676.
[40] American Concrete Institute (2014).
[41] M. Hussein Abdallah, M. Shazly, H.M. Mohamed, R. Masmoudi, A. Mousa, Nonlinear finite element analysis of short and long reinforced concrete columns confined with GFRP tubes, J. Reinf. Plast. Compos. 36 (13) (2017) 972–987.
[42] A. Jawdhari, A. Fam, Numerical study on mechanical and adhesive splices for ribbed GFRP plates used in concrete beams, Eng. Struct. 174 (2018) 478–494.
[43] K. William E. Warnke Constitutive model for the triaxial behavior of concrete international association for bridge and structure engineering proceedings 1975 Bergamo.
[44] L.C. Hollaway, M.B. Leeming (Eds.), Strengthening of reinforced concrete structures, Woodhead Publishing Limited, 1999.
[45] S.H. Lo, A.K.H. Kwan, Y. Ouyang, J.C.M. Ho, Finite element analysis of axially loaded FRP-confined rectangular concrete columns, Eng. Struct. 100 (2015) 253–263.
[46] O. Youssf, M.A. ElGawady, J.E. Mills, X. Ma, Finite element modelling and dilation of FRP-confined concrete columns, Eng. Struct. 79 (2014) 70–85.
[47] M. Thériault, K.W. Neale, S. Claude, Fiber-reinforced polymer-confined circular concrete columns: Investigation of size and slenderness effects, J. Compos. Constr. 8 (4) (2004) 323–331.
[48] L. Ombres Confinement effectiveness in concrete strengthened with fiber reinforced cement based composite jackets FRPCS-8. 2007 Patras, Greece.
[49] A. D'Ambrisi, L. Feo, F. Focacci, Experimental analysis on bond between PBO-FRCM strengthening materials and concrete, Compos. B Eng. 44 (1) (2013) 524–532.
[50] G.E. Thermou, K. Katakalos, G. Manos, Concrete confinement with steel-reinforced grout jackets, Mater. Struct. 48 (5) (2015) 1355–1376.